Simple ultraviolet calibration source with reference spectra and its use with the Galileo orbiter ultraviolet spectrometer

J. M. Ajello, D. E. Shemansky, B. Franklin, J. Watkins, S. Srivastava, G. K. James, W. T. Simms, C. W. Hord, W. Pryor, W. McClintock, V. Argabright, and D. Hall

We have developed a simple compact electron impact laboratory source of UV radiation whose relative intensity as a function of wavelength has an accuracy traceable to the fundamental physical constants (transitions probabilities and excitation cross sections) for an atomic or molecular system. Using this laboratory source, calibrated optically thin vacuum ultraviolet (VUV) spectra have been obtained and synthetic spectral models developed for important molecular band systems of H_2 and N_2 and the $n\ {}^1P^0$ Rydberg series of He. The model spectrum from H_2 represents an extension of the molecular branching ratio technique to include spectral line intensities from more than one electronic upper state. The accuracy of the model fit to the VUV spectra of H_2 and N_2 is sufficient to predict the relative spectral intensity of the electron impact source and to serve as a primary calibration standard for VUV instrumentation in the 80–230-nm wavelength range. The model is applicable to VUV instrumentation with full width at half-maximum ≥ 0.4 nm. The present accuracy is 10% in the far ultraviolet (120–230 nm), 10% in the extreme ultraviolet (EUV) (90–120 nm), and 20% in the EUV (80–90 nm). The $n\ {}^1P^0$ Rydberg series of He has been modeled to 10% accuracy and can be considered a primary calibration standard in the EUV (52.2–58.4 nm). A calibrated optically thin spectrum of Ar has been obtained at 0.5-nm resolution and 200-eV electron impact energy to 35% accuracy without benefit of models over the EUV spectral range of 50–95 nm. The Ar spectrum expands the ultimate range of the VUV relative calibration using this source with the four gases, He, Ar, H_2, and N_2, to 50–230 nm. The calibration of the Galileo orbiter ultraviolet spectrometer for the upcoming Jupiter mission has been demonstrated and compared to results from other methods.

I. Introduction

Primary and secondary standards of absolute spectral radiance with uncertainties of <10% in the vacuum ultraviolet (VUV) from 50 to 250 nm include the argon mini[1] and maxi[2] arcs, the synchrotron,[3,4] the deuterium lamp,[5,6] and the hydrogen arc discharge.[2,7–9] Prior to 1980 the argon mini arc was the only small compact laboratory source available for general laboratory use below 170 nm with a short-wavelength cutoff of ~114 nm, depending on window material. The small portable deuterium lamp has had its short-wavelength calibration edge brought down to 115 nm extending its wavelength range of applicability to include all wavelengths between 115 and 350 nm.[5,6] Both the argon mini arc and the deuterium lamp are calibrated against the hydrogen arc. The hydrogen arc is a primary standard of reference. This method is based on the assumption that the hydrogen plasma is in local thermodynamic equilibrium. The hydrogen arc is complicated and requires a 1200-V 100-A dc power supply.[2] To meet the lack of portable transfer standards in the far ultraviolet (FUV) the argon mini arc secondary standard was developed. A power supply of 1.2 kW is normally required. By contrast the principal power requirement for the simple electron source controller described here is the dc filament power supply of 2.5 V at 2 A. Degradation of optics from intense EUV radiation is absent. The uniformity of the source eliminates the need for field apertures as required in other

---

D. Hall and D. E. Shemansky are with University of Arizona, Lunar & Planetary Laboratory, Tucson, Arizona 85721; V. Argabright, W. McClintock, W. Pryor, and C. W. Hord are with University of Colorado, Department of Astrophysical, Planetary & Atmospheric Science, Laboratory for Atmospheric & Space Physics, Boulder, Colorado 80309; the other authors are with California Institute of Technology, Jet Propulsion Laboratory, Pasadena, California 91109.

Received 6 April 1987.
0003-6936/88/050890-25$02.00/0.

spectral irradiance calibrations. This source provides a traceable reference for VUV calibrations concerned with temporal variation in instrument response.

Many UV calibration requirements are satisfied with a relative calibration of sensitivity and wavelength. The absolute calibration for laboratory and spaceborne spectrometers including detectors can be determined by normalization by other means: (1) comparison to a blackbody standard for $\lambda > 180$ nm at a single point[9]; (2) a calibrated photodiode in conjunction with a predispersed lamp source[10]; (3) electron–photon coincidence method of McAdams and Srivastava[11]; (4) the electron impact induced fluorescence method in which known atomic or molecular cross sections are utilized to define absolute emission rates at particular wavelengths. The most important transitions for method (4) in the UV are the H Ly-α[13] produced by dissociative excitation of H_2, the 58.4-nm transition[14] from He, and the 120.0-nm transition[15] from dissociative excitation of N_2.[12]

In the early 1970s several authors quantified the use of the molecular branching ratio technique for use in the VUV as a relative calibration source.[12,16,17] Mumma[12] proposed VUV band systems of N_2, H_2, CO, NO, and NO^+. These band systems are composed of closely spaced vibrational features ideal for a mapping structure in a relative calibration. However, Mumma limited the use of the H_2 many line spectrum to twenty-eight rotational lines from the B state and to high-resolution studies of the Q branches from the C state. In practice the recommended $CO(A\ ^1\Pi \rightarrow X^1\Sigma^+)$ fourth positive band system is suitable for calibration because the electronic transition moment has been measured.[12] Our laboratory spectra of NO ($A\ ^2\Sigma^+ \rightarrow X\ ^2\Pi$) and NO^+ ($A\ ^1\Pi \rightarrow X\ ^1\Sigma^+$) indicate that these band systems are not practical because of blending with at least four other systems. In the intervening years the N_2 LBH ($a\ ^1\Pi_g - X\ ^1\Sigma_g^+$) transition has been the only system used for calibration.[15,18] This band system has many advantages[15]: (1) no measurable cascade (<5%); (2) intense and regularly spaced (every ~2.0 nm) features from 127 to 230 nm; (3) minimal blending with NI features; (4) narrow [$\lesssim$0.05-nm full width at half-maximum (FWHM)] rotational structure at 300 K; (5) variation in electronic transition moment of <5%.[12,15,19] An experimenter must exercise the following caveats[12,15]: (1) background pressures of $<10^{-4}$ T; (2) characteristic path length of several centimeters and wide field of view must be available because of the 80-μs lifetime of the transition; (3) electron energies, $\epsilon > 30$ eV, need to be employed due to threshold effects.[15] Experimenters calibrating spaceborne VUV instrumentation have not taken advantage of this simple technique using the LBH bands. Part of this reticence lies in the fact that many laboratories do not have a suitable electron-beam calibration source.

We describe a relative calibration technique that expands the work of Mumma *et al.*,[12] Aarts *et al.*,[16] and McConkey[17] and allows a relative calibration to accuracies of 5–20% over the 80–230-nm wavelength range and to an accuracy of 35% in the 50–80-nm range. This laboratory technique applied to the problem of calibration of a UV spectrometer with known instrumental transmission function requires (1) the design and construction of a suitable low-energy electron beam (10–500 eV) crossed with a molecular beam; (2) a computer file of emission intensity vs wavelength and electron energy for readily available gases: He, Ar, H_2, and N_2. We have developed a model of $N_2(a\ ^1\Pi_g \rightarrow X\ ^1\Sigma_g^+)$ molecular band intensities, H_2 (Rydberg) rotational line intensities, and He $n\ ^1P^0$ atomic line intensities for convolution with the instrument transmission function. The computer file listing of LBH band intensities has been previously published[15] and consists of ~100 strong bands extending from 127 to 230 nm. A few weaker bands exist up to 260 nm. The H_2 spectrum consists of ~70,000 rotational lines from H_2 electronic transitions as well as Ly-α and Ly-β, and as such the H_2 line intensity model is too long to be published or to be useful for a microcomputer laboratory installation. Instead we give a listing of a model medium-resolution (0.025-nm) 100-eV H_2 spectrum which can be further convoluted with the actual instrument transmission function for applications where FWHM $\geq$ 0.4 nm. The low-resolution H_2 spectrum is now well understood, and broad instrument resolution (FWHM $\geq$0.4 nm) need not be considered a problem in the calibration. High-resolution studies of the unperturbed Q branch or P, R branches of the Π^- states need not be carried out for calibration purposes. We make use of our laboratory studies and models of the He $n\ ^1P^0$ Rydberg series excitation cross sections[14] to list line intensities for $n = 2,3,4$ of the He spectrum from 52.2 to 58.4 nm.

The synthetic spectra are based on the instrumental spectral transmission function convolved with calculated discrete transitions. These data files based on fundamental atomic and molecular constants for He, N_2, and H_2 constitute a primary standard of reference for the 52.2–58.4- and 80–230-nm wavelength range. We provide electron impact-induced fluorescence spectra at 0.5-nm resolution and 200-eV impact energy that allow calibration over the 50–80-nm wavelength range. A calibration of a UV spectrometer with the electron impact source described in this paper provides an accurate in-house laboratory calibration method that is more practical than acquiring guest investigator time at the National Bureau of Standards (NBS) facility for a primary calibration source or at a regional synchrotron source. The calibration method described here has been applied to the Galileo orbiter ultraviolet spectrometer to demonstrate the agreement of this calibration technique with other more traditional methods. The H_2 cross sections for the H_2 Rydberg series, $^1\Sigma_u^+\ np\sigma$ and $^1\Pi_u\ np\pi$, with $n = 2,3,4$ have been recalculated. These are the electronic states that produce the H_2 many line spectrum. In the following text we first describe the magnetically confined electron-beam source followed by the experimental and synthetic calibration spectra of H_2, N_2, and He required for evaluation.

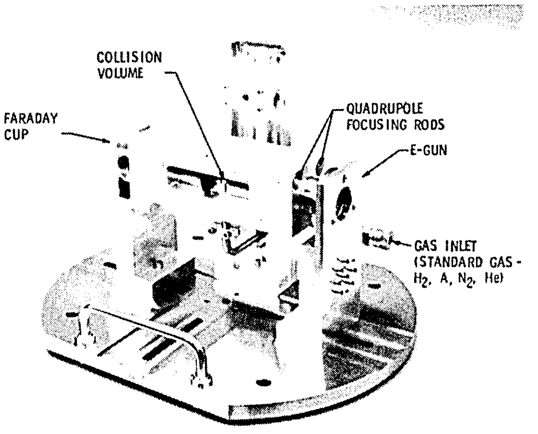

Fig. 1. Electron gun and molecular beam collimated hole structure which produce an orthogonal electron beam and molecular beam. The collision volume represents the interaction area for inelastic electron atom/molecule collisions. The head gas pressure to the molecular beam is read with a baratron. The mechanical yolk for the permanent magnet had a center-to-center spacing of the magnets of 3.75 cm (1.50 in.), and for the electromagnet the center-to-center spacing of the magnet was 5.7 cm (2.25 in.).

II. Electron Impact Calibration Source

Magnetic collimation has been used in the past[20] for generating low-energy (10–500-eV) high-current (10–500-μA) collimated electron beams. We have used a magnetically confined electron beam in the UV calibration of spectrometers[14,15,18,21] and in the study of electron atom/molecule collisions.[4,15,18,21,22] The important components of the crossed beam instrumentation are indicated in Fig. 1. For further detail we show in Fig. 2 an assembly drawing of the electron gun with the scale of the axial magnetic field as a function of distance indicated in the plot. The entire source is compact (~15.0-cm maximum dimension) and vacuum compatible and presents a large field of view for observing the collision region, ~4 cm × 10 cm, unobscured.

The electron-beam source is shown in Fig. 1 with a permanent magnet quadrupole configuration which collimates the electron beam with a 50–200-G axial field. Each magnet has equal pole strength and is placed so that all the north poles occupy one end of the rectangular housing. We have built and tested a similar electromagnetic quadrupole (four solenoids with soft iron core). A plot of the axial magnetic field produced by the electromagnet with a current of 0.9 A

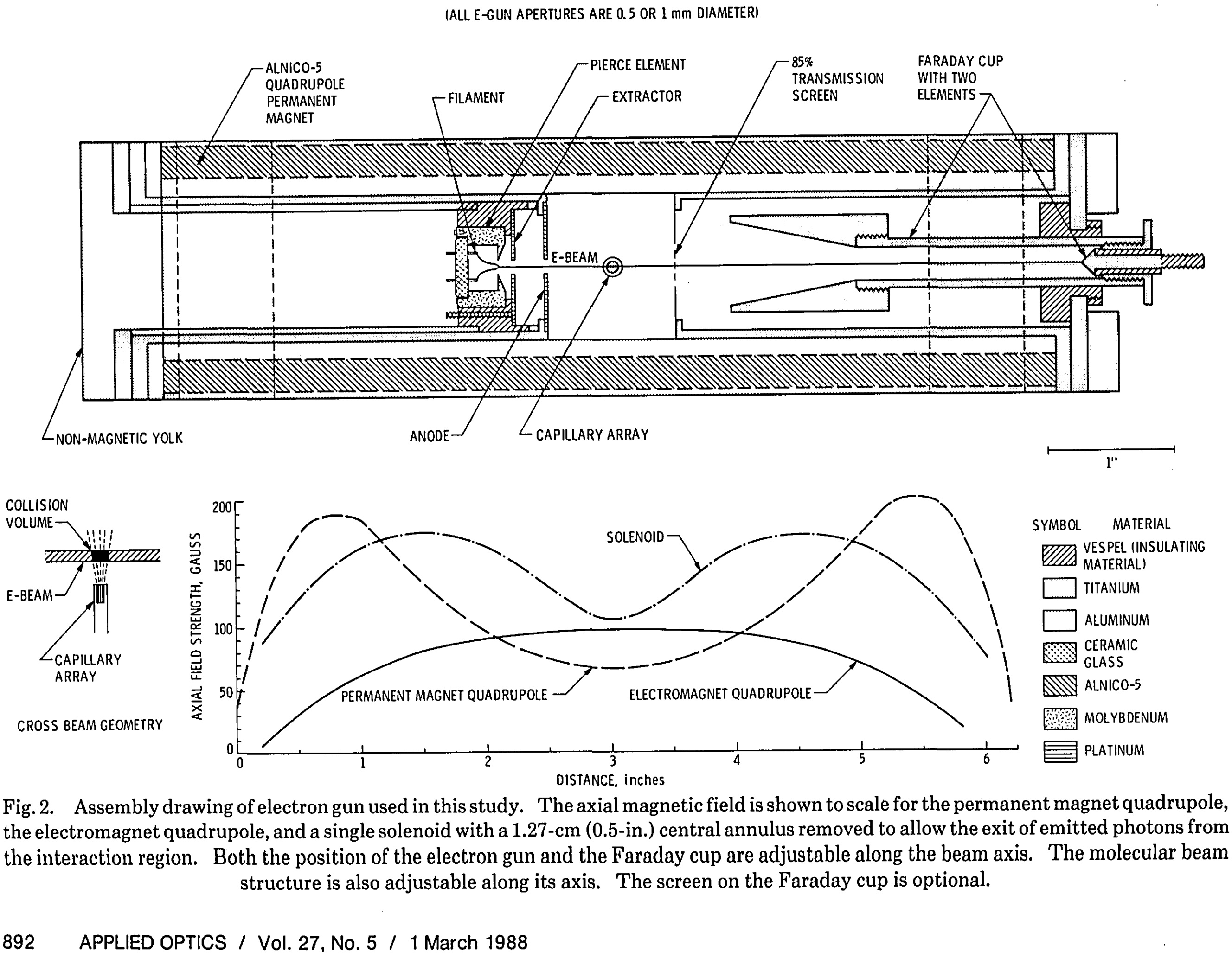

Fig. 2. Assembly drawing of electron gun used in this study. The axial magnetic field is shown to scale for the permanent magnet quadrupole, the electromagnet quadrupole, and a single solenoid with a 1.27-cm (0.5-in.) central annulus removed to allow the exit of emitted photons from the interaction region. Both the position of the electron gun and the Faraday cup are adjustable along the beam axis. The molecular beam structure is also adjustable along its axis. The screen on the Faraday cup is optional.

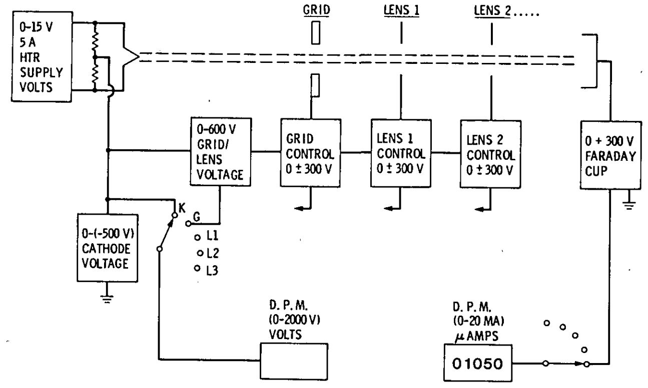

Fig. 3. Block diagram of the electronics for operating the electron gun. Note that all lenses are referenced with respect to the center of the filament. Extra lens element connections are available.

flowing in each solenoid is also shown in Fig. 2. The magnetic field of the electromagnet is considerably more uniform over the path length of the electron beam. However, either configuration produces an axially symmetric magnetic field adequate for the collimation of the low-energy electron beam. The design of the magnetic quadrupole is similar to that published by Taylor *et al.*[23] who used four permanent magnets held together in a mechanical yolk. However, our design does not use ferrous pole caps, and thus the magnetic field is analytically derivable. A complete mathematical description of the axial magnetic field from a magnetic quadrupole is given in the Appendix, a consideration in the design and testing of a magnetic collimator. The electron gun and Faraday cup are immersed in the magnetic field (see Fig. 2). The axes of the electron gun and Faraday cup coincide with the axis of symmetry of the magnetic field. The electrons are produced by heating a pure tungsten filament or thoriated tungsten, the center of which is the cathode. The electron gun is a two-stage gun which utilizes an extractor stage to overcome the space charge in front of the cathode and an anode stage to achieve the final energy. A block diagram of the electronics is shown in Fig. 3. A detailed drawing of the electronics for controlling the energy and current of the electron beam is shown in Fig. 4.

Electrons are extracted from the filament region by a Pierce electrode and extractor lens combination which serves as the first stage.[20,24] These electrons then follow axial lines of force. They are accelerated or declerated by an aperture lens or anode which serves as the second stage. The anode is electrically connected to ground. The energy of the electrons is selected by varying the bias on the filament with respect to ground. The energy spread of the beam is equal to the thermal energy (0.26 eV). The transverse kinetic energy for the case of a uniform axial magnetic field and

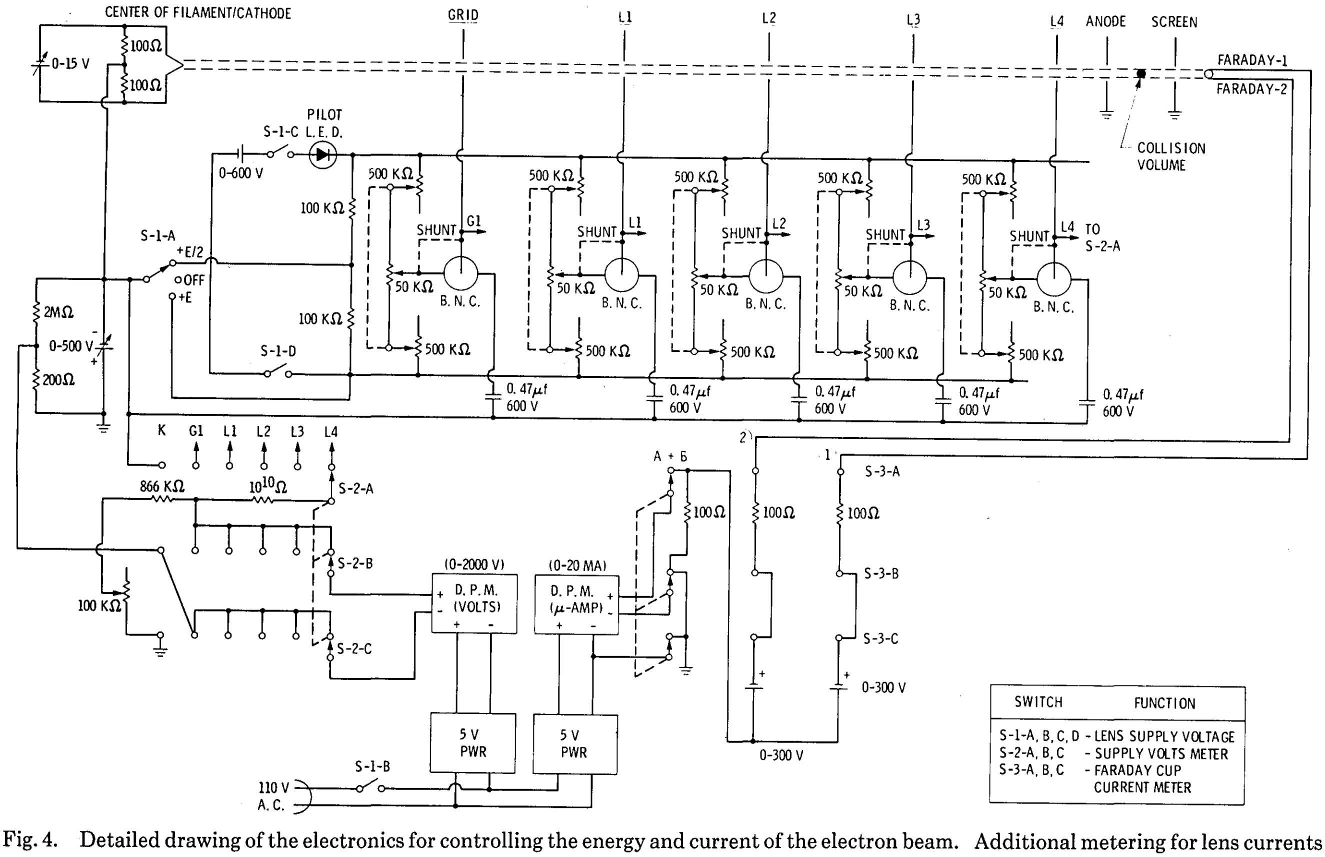

SWITCH	FUNCTION
S-1-A, B, C, D	- LENS SUPPLY VOLTAGE
S-2-A, B, C	- SUPPLY VOLTS METER
S-3-A, B, C	- FARADAY CUP CURRENT METER

Fig. 4. Detailed drawing of the electronics for controlling the energy and current of the electron beam. Additional metering for lens currents is available at BNC connections, which are provided. Normally the Pierce element has a potential of 1 or 2 V positive with respect to the cathode, and the extractor has a potential of 10–50 V positive with respect to the cathode. A smaller voltage lens power supply than shown in the drawing is perfectly suitable.

negligible transverse electric fields is determined by the thermal energy of the heated filament. The radius of gyration is 0.17 mm for electrons with a transverse component of kinetic energy equal to the thermal energy. The increase in path length through the interaction region is <2% for all accelerating energies of interest (10–500 eV). A more detailed discussion of thermal effects in a nonuniform magnetic field is given in Ref. 23. The electron-beam calibration source has been found to provide a steady source of current for days at a time. To generate an energy selected beam of high resolution (~0.1 eV) one can replace the electron gun described above by a trochoidal monochromator[25] or a retarding potential difference type.[26]

The electron beam is monitored by a Faraday cup with a design optimized to minimize backscattered secondary electrons generated in the cup. A voltage bias is applied to the collecting electrode of the cup. This voltage is varied until the collected electron current reaches a saturation value, a value of 90–100% of the cathode power supply current. An additional electrode at a 45° angle to the magnetic field has a separate potential applied to increase the capability to trap secondary electrons. The ability of the Faraday cup to prevent escape of secondary electrons has been verified by measurement of the N_2 ($a\,^1\Pi_g \rightarrow X\,^1\Sigma_g^+$) optically forbidden excitation function.[15] A small amount of escape of secondary electrons would have no effect on the calibration spectra presented here.

The electron beam passes through the collision region optionally configured as a static chamber or as a crossed beam system. A gas beam is generated using a multichannel capillary array or a hypodermic needle to form a 1-mm^3 collision volume.[12] The magnetic field structure also permits the placement of a crucible which can be heated to produce beams of such materials as sodium or potassium, for example. Mechanical allowance for three-axis manipulation of the capillary array to steer the gas beam is recommended for optimum alignment of the gas beam with respect to the electron beam. Optimum alignment can be tested by optical means.

For crossed beam work, the capillary array design produces a high-density molecular beam in the collision region. Each tube in the capillary array (~105 in total) has a length of 0.292 cm and a diameter of 50 μm. The density distribution expected in the collision region crossed electron beam and molecular beam geometry is discussed in Ref. 27.

The density distribution has a strong forward peak with a distribution that depends on head pressure (gas pressure behind capillary array, see Fig. 1) and aspect ratio (d/L, where d is tube diameter and L is tube length). In brief the larger the aspect ratio and/or head pressure the larger the angular FWHM of the molecular beam. Typical beam densities for this capillary array are ~10^{13} cm^3 on the beam axis for 1-Torr head pressure.

A typical photon flux expected from the electron impact source at 100 eV produced by dissociative excitation of H_2 with an electron beam current of 300 μA is, for example, for H Ly-α:

$$4\pi I = \frac{QNLi}{e} \simeq 10^{10}\ \text{photons/s}, \tag{1}$$

where $4\pi I$ is photon flux in all directions in photons/s;
Q is the dissociative excitation cross section of H_2 and equals 7.3×10^{-18} cm^{-2} (See Ref. 13);
N is the density in the collision region, ~10^{13} cm^3;
L is the path length of the electron in the collision region, ~10^{-1} cm;
i is the electron-beam current, ~300 μA; and
e is the charge on the electron.

At the entrance slit to the spectrometer located 25 cm from the source region, the spectral irradiance is ~1×10^6 photons/cm^{2}s. For an entrance slit of 4- × 0.1-mm dimension, the incident photon flux entering the spectrometer is 5×10^3 photons/s. The main drawback of the electron-beam source brought out from this calculation is that the spectral irradiance is several orders of magnitude weaker than the other VUV calibration lamps mentioned in the introduction. Photon counting techniques are a requirement.

III. Reference Spectra

For the source we have just described, the relative band intensities from a single electronic state of most diatomic molecules excited by electron impact at low pressure are accurately determined by Franck-Condon factors or transition probabilities. The relative intensity $I_{v'v''}$ of a band system can be written[12]

$$I_{v'v''} = \frac{Q_{v'}}{Q}\frac{A_{v'v''}}{A_{v'}}, \tag{2}$$

where $Q_{v'}$ and Q are excitation cross sections to level v' and to all levels, respectively, $A_{v'v''}$ is the emission transition probability for band $v'v''$, and $A_{v'}$ is the total transition probability (emission + predissociation). $I_{v'v''}$ is normalized and sums to unity for a band system with negligible predissociation. However, for the B'', D, and D' electronic states of H_2, predissociation is important.[13,21] In the Born limit

$$\frac{Q_{v'}}{Q} = \frac{\lambda^3_{v'0}A_{v'0}}{\sum\lambda^3_{v'0}A_{v'0}}, \tag{3}$$

where $\lambda_{v'0}$ is the wavelength of the band (v',0). This ratio is achieved to within 5% for the LBH bands of N_2 at 50 eV. However, in the case of H_2, the threshold energies[13] for the levels v' are sufficiently separated to show deviations (~5%) from Eq. (3) at 100 eV, and this is taken into account in the models.

In the case of the N_2 LBH system, in which the electronic transition moment is constant, we write $\lambda^3_{v'o}A_{v'o} \propto q_{v'o}$, and the equation for $I_{v'v''}$ simplifies to

$$I_{v'v''} = \frac{q_{v'o}A_{v'v''}}{A_{v'}} = q_{v'o}\frac{\dfrac{q_{v'v''}}{\lambda^3_{v'v''}}}{\sum_{v''}\dfrac{q_{v'v''}}{\lambda^3_{v'v''}}}, \tag{4}$$

where $q_{v'v''}$ is the Franck Condon factor between vibrational levels v' and v''.

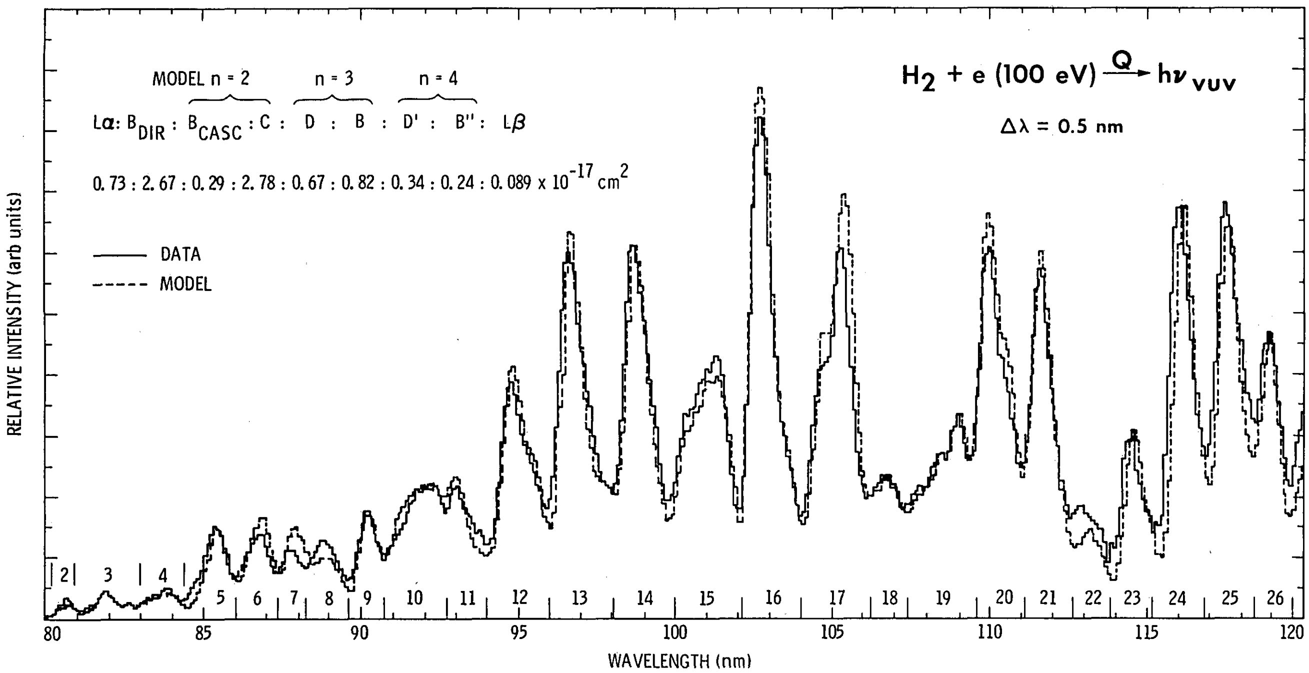

Fig. 5. Laboratory spectrum at 0.5-nm resolution observed at 100 eV and best model fit for the EUV region. The twenty-nine consecutive numbered areas used for a calibration comparison are discussed in the text. The ratios of the electronic cross sections to Ly-α are indicated.

We assemble the necessary normalized relative intensities, $I_{v'v''}$ vs $\lambda_{v'v''}$, in table form to facilitate calibration. The table is to be used as a data file input to a convolution integral program, individually tailored for the instrument slit or transmission function. In the case of H_2 we will give the quantity

$$I(\lambda) = \sum_{\substack{\text{all}\\ \text{lines}\\ \lambda \text{ to } \lambda + \Delta\lambda}} \int I_{j,i,v_j,v_i}(\lambda')S(\lambda,\lambda',\Delta\lambda)d\lambda', \qquad (5)$$

where S is a spectral transmission function of FWHM $= \Delta\lambda = 0.025$ nm, and $I(\lambda)$ is the integrated spectral intensity determined by a convolution integral of each rotational line (j, $v_j \rightarrow i$, v_i) followed by a sum over all lines in the interval λ to $\lambda + \Delta\lambda$. The detailed description of I_{j,i,v_j,v_i} is given in Ref. 21.

A low-pressure background gas environment to the collision source region is required to preclude effects of secondary collisions or self-absorption. The N_2 spectrum extends from 127 to 260 nm, the H_2 spectrum from 80 to 170 nm, and He from 52.5 to 58.4 nm. Ionization excitation of Ar I between 50 and 95 nm leads to a rich extreme ultraviolet (EUV) spectrum between 50 and 95 nm. These four gases in principle allow a relative calibration in the 50–230-nm range.

The use of spectral line intensities in the VUV to determine cross sections has developed through the use of the branching ratio technique[28] in transitions with the same upper state. These transitions are defined in relative intensity by known transition probabilities. The relative population of the state is then irrelevant to the calibration process. The technique can be applied to either atomic or molecular transitions.[12] We propose to expand the technique by using transitions with known upper state relative populations, allowing an expanded spectral range to be examined.

IV. Hydrogen

The H_2 Rydberg band systems have been modeled in fine structure detail using accurate transition probabilities[29] and cross sections. This provides a reference spectrum for calibration over the 80–165 nm range. The H_2 Lyman B and Werner systems C dominate the 95–165 nm region, and the higher Rydberg band systems become important at wavelengths below 110 nm in the EUV. We have recently modeled a 100-eV EUV spectrum in Ref. 21 to determine the ratio of higher Rydberg ($n = 3{,}4$, where n is the principal quantum number) state cross sections. The Rydberg state cross sections were reevaluated using recent calculations of the transition probabilities of the D state and B' state[30] and the spectrum in Fig. 5. The present spectrum (Fig. 5) has a higher signal-to-noise ratio (SNR $\sim 10^5$ at Ly-α) and was obtained at lower foreground abundances, 7×10^{12} cm^2, than the EUV spectrum in Ref. 21. The model fit to the laboratory spectrum was obtained by a least-squares scaling of each modeled electronic system. The revised Rydberg state cross sections and Lyman-α cross section along with the previously published Lyman and Werner band system cross sections are given in Table I. This table updates previous cross sections given in Ref. 13.

The model spectra based on these tables are moderately complicated and consist of nearly 70,000 rotational lines from seven electronic states of H_2 as well as Ly-α and Ly-β. It is impractical to present a computer file listing. Instead we show in Fig. 6(a) a typical moderate-resolution (0.025-nm) model spectrum of H_2 from 90 to 100 nm. This spectrum was obtained by convoluting a 0.025-nm triangular transmission function with the many line rotational model spectrum of H_2 in Ref. 21. In Table II we have a listing of this high-resolution spectrum in steps of 0.025 nm. The spectrum (80–170 nm) may be obtained by the user over the SPAN network or on an IBM floppy disk by contacting one of us (J.A.).

To obtain a model spectrum for calibration it is only necessary to convolute the 0.025-nm spectrum in Table II with the instrumental FWHM. The resultant spectrum has the actual FWHM $\Delta\lambda$ of the instrument to be calibrated. The 0.025-nm step size integrated intensity acts effectively as a delta function when convoluted with the instrumental slit function for $\Delta\lambda \geq 0.4$ nm. We show in Fig. 6(b) the convolution of the 90–100-nm spectrum of Fig. 6(a) with a 0.5-nm slit function. The result is a close approximation to the convolution of the many lined rotational spectrum with the same 0.5-nm triangular slit function. The two spectra obtained by the different convolutions at 0.5-nm resolution are compared in Fig. 6(b). The variation of the H_2 Rydberg system cross sections with energy in the laboratory domaine requires that the intensity factors in Table II be limited to data obtained only at 100 eV. An additional reason for the requirement $\Delta\lambda \geq 0.4$ nm is to ensure that rotational or vibrational perturbations have no effect on the model spectrum except for one or two cases to be discussed. One basic result of this analysis is that the broad intensity distribution is unaffected in spite of the many known perturbations[32] to the rotational energy levels of various electronic Rydberg states of H_2. H_2 rotational perturbation effects produce energy level shifts that lead to displacement of the rotational line up to 0.01 nm from the unperturbed rotational line. This positional effect is only resolvable at high resolution. The first high-resolution line intensity studies of rotational perturbations on the *B* and *C* states have been carried out by Abgrall *et al.*[33] At this resolution perturbations of an individual line intensity may be significantly different from the model prediction. However, the sum of transition probabilities of each pair of affected rotational levels must be the same with and without the perturbations.

We illustrate the use of the electron excited H_2 spectrum as a calibration source in Fig. 5. Figure 5 shows a plot of model and data in the EUV region at 0.5-nm resolution. The calibration of the experimental EUV spectrum in Fig. 5 is based on a double monochromator method from 80 to 110 nm. The calibration of the wavelength region longward of 110 nm is ultimately based on the N_2 molecular branching ratio technique and subsequently on the Lyman and Werner band experimental cross-section measurements. When we compare the model and the EUV data, calibrated with the double monochromator method, the fit is excel-

Table I. Absolute Cross Sections of the Rydberg Systems, H Ly-α, H Ly-β and E, F Systems at 100 eV

State	Excitation Cross Sections (10^{-17} cm^2) at 100 eV A*	Excitation Cross Sections (10^{-17} cm^2) at 100 eV B+	Emission Cross Section*
H(2p)	0.73	0.82	0.73
H(3p)	0.064	0.089	0.064
$B\,^1\Sigma_u^+$	2.67	2.67	2.67
$B'\,^1\Sigma_u^+$	0.82	0.51	0.82
$B''\,^1\Sigma_u^+$	0.25	0.15	0.0083
$C\,^1\Pi_u$	2.78	2.78	2.78
$D\,^1\Pi_u$	0.67	0.55	0.47
$D'\,^1\Pi_u$	0.34	0.22	0.19
$E,F\,^1\Sigma_g^+$	0.29	0.29	0.29

*A This work and Ref. 13, 18, 31 and Glass-Maujean (private communication).

+B Ref. 13.

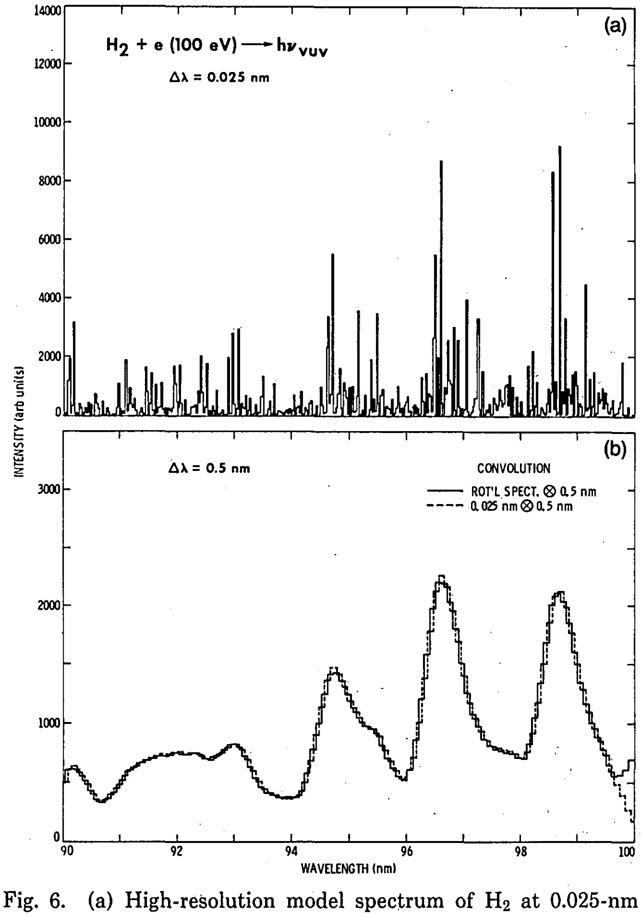

Fig. 6. (a) High-resolution model spectrum of H_2 at 0.025-nm resolution from 90 to 100 nm. (b) Comparison of low-resolution model spectra at 0.5 nm obtained by convolution of 0.5-nm triangular slit function with (a) and with many-line rotational spectrum.

Table II. High-Resolution (0.025-nm) Spectrum of H_2 from 90 to 130 nm at 100 eV for Calibration at $\Delta\lambda \geq 0.4$ nm

INTEGRATED INTENSITY λ TO $\lambda \mp \Delta\lambda$ (arb units)

λ WAVE-LENGTH (A)	$\Delta\lambda$→ 0.0	0.25	0.50	0.75	1.00	1.25	1.50	1.75
900.	0.319E+02	0.115E+03	0.205E+00	0.119E+04	0.200E+04	0.786E+02	0.146E+03	0.146E+04
902.	0.194E+04	0.106E+02	0.106E+03	0.664E+02	0.564E+03	0.279E+02	0.342E+02	0.356E+03
904.	0.889E+02	0.449E+03	0.271E+00	0.232E+03	0.218E+03	0.361E+02	0.294E+02	0.103E+04
906.	0.148E+03	0.226E+03	0.440E+01	0.293E+02	0.471E+03	0.405E+02	0.756E+02	0.309E+03
908.	0.280E+01	0.564E+01	0.503E+02	0.728E+02	0.305E+01	0.156E+02	0.257E+03	0.109E+04
910.	0.458E+02	0.673E+02	0.213E+03	0.187E+04	0.886E+02	0.197E+03	0.222E+03	0.128E+04
912.	0.349E+03	0.570E+03	0.232E+03	0.641E+01	0.110E+02	0.471E+02	0.225E+03	0.169E+03
914.	0.497E+02	0.128E+04	0.121E+04	0.148E+01	0.520E+00	0.446E+03	0.147E+04	0.192E+03
916.	0.319E+03	0.760E+03	0.319E+03	0.181E+03	0.124E+04	0.166E+03	0.237E+03	0.966E+02
918.	0.232E+03	0.317E+02	0.353E+03	0.159E+03	0.407E+03	0.142E+03	0.266E+04	0.201E+03
920.	0.498E+03	0.141E+03	0.175E+04	0.453E+03	0.284E+02	0.394E+03	0.161E+03	0.544E+02
922.	0.504E+02	0.363E+03	0.368E+02	0.464E+03	0.440E+03	0.137E+03	0.437E+03	0.473E+03
924.	0.178E+04	0.152E+04	0.193E+02	0.339E+03	0.276E+03	0.162E+04	0.185E+03	0.674E+02
926.	0.180E+03	0.229E+03	0.119E+03	0.868E+03	0.925E+02	0.424E+00	0.110E+03	0.215E+03
928.	0.112E+02	0.133E+01	0.572E+02	0.195E+04	0.579E+02	0.130E+03	0.878E+03	0.207E+04
930.	0.332E+03	0.533E+01	0.312E+04	0.151E+03	0.445E+03	0.962E+01	0.406E+03	0.852E+03
932.	0.430E+02	0.221E+03	0.614E+03	0.193E+01	0.841E+01	0.132E+03	0.395E+03	0.256E+02
934.	0.537E+02	0.156E+03	0.725E+03	0.121E+04	0.170E+03	0.141E+02	0.313E+02	0.234E+02
936.	0.757E+03	0.791E+02	0.417E+01	0.299E+03	0.867E+03	0.706E+02	0.197E+03	0.196E+03
938.	0.151E+03	0.613E+02	0.711E+02	0.117E+03	0.417E+02	0.316E+03	0.592E+01	0.262E+03
940.	0.135E+03	0.911E+03	0.180E+01	0.129E+03	0.581E+03	0.968E+02	0.856E+03	0.628E+01
942.	0.750E+02	0.203E+02	0.440E+03	0.624E+02	0.793E+02	0.432E+03	0.490E+03	0.551E+02
944.	0.262E+01	0.430E+03	0.319E+02	0.243E+02	0.316E+02	0.127E+04	0.122E+03	0.116E+03
946.	0.863E+03	0.504E+04	0.645E+02	0.410E+03	0.786E+03	0.560E+04	0.826E+02	0.226E+03
948.	0.188E+03	0.140E+04	0.111E+04	0.209E+03	0.631E+02	0.196E+04	0.637E+02	0.650E+03
950.	0.290E+03	0.805E+03	0.313E+03	0.745E+03	0.283E+03	0.253E+03	0.406E+04	0.289E+01
952.	0.254E+02	0.142E+03	0.188E+03	0.727E+03	0.132E+02	0.181E+01	0.249E+02	0.157E+04
954.	0.640E+03	0.640E+03	0.300E+03	0.134E+04	0.261E+04	0.533E+01	0.256E+03	0.133E+04
956.	0.120E+03	0.415E+02	0.262E+03	0.358E+03	0.268E+03	0.300E+01	0.103E+03	0.611E+03
958.	0.716E+01	0.100E+03	0.354E+03	0.134E+04	0.204E+03	0.207E+00	0.308E+03	0.398E+03
960.	0.522E+03	0.185E+02	0.720E+03	0.114E+03	0.167E+03	0.252E+02	0.416E+03	0.485E+02
962.	0.634E+02	0.226E+03	0.467E+02	0.113E+04	0.726E+03	0.121E+01	0.711E+03	0.850E+03
964.	0.261E+03	0.126E+04	0.107E+03	0.582E+02	0.816E+04	0.219E+02	0.999E+03	0.107E+04
966.	0.853E+04	0.635E+03	0.738E+01	0.235E+03	0.141E+04	0.178E+04	0.138E+04	0.932E+03
968.	0.102E+04	0.129E+04	0.185E+04	0.941E+02	0.222E+04	0.634E+03	0.629E+02	0.219E+03
970.	0.197E+03	0.344E+03	0.401E+04	0.423E+02	0.141E+03	0.736E+01	0.120E+03	0.242E+03
972.	0.891E+03	0.451E+03	0.256E+04	0.920E+03	0.171E+03	0.156E+04	0.436E+01	0.746E+02
974.	0.208E+02	0.322E+03	0.401E+03	0.594E+02	0.132E+03	0.627E+03	0.455E+03	0.224E+01
976.	0.248E+03	0.126E+04	0.160E+03	0.757E+03	0.810E+02	0.141E+04	0.864E+02	0.104E+04
978.	0.563E+03	0.121E+04	0.100E+04	0.100E+03	0.678E+00	0.692E+03	0.296E+02	0.133E+03
980.	0.511E+03	0.787E+01	0.576E+02	0.192E+02	0.172E+02	0.138E+04	0.379E+03	0.472E+02
982.	0.117E+04	0.123E+04	0.341E+03	0.117E+04	0.629E+01	0.342E+02	0.215E+03	0.136E+03
984.	0.223E+03	0.142E+03	0.614E+02	0.129E+04	0.263E+03	0.611E+03	0.259E+03	0.836E+04
986.	0.501E+03	0.995E+03	0.122E+03	0.900E+04	0.246E+03	0.520E+02	0.129E+04	0.166E+04
988.	0.170E+04	0.300E+03	0.734E+03	0.107E+04	0.144E+04	0.266E+02	0.973E+02	0.248E+04
990.	0.252E+01	0.346E+03	0.411E+03	0.369E+02	0.311E+02	0.268E+02	0.471E+04	0.293E+03
992.	0.129E+04	0.287E+00	0.611E+02	0.178E+04	0.976E+01	0.111E+03	0.846E+03	0.261E+03
994.	0.217E+03	0.618E+03	0.120E+04	0.235E+02	0.942E+03	0.355E+03	0.628E+02	0.106E+03
996.	0.411E+03	0.415E+03	0.287E+02	0.855E+02	0.469E+02	0.139E+03	0.783E+03	0.191E+04
998.	0.179E+01	0.772E+02	0.631E+02	0.315E+02	0.287E+03	0.259E+02	0.217E+01	0.137E+01
1000.	0.403E+03	0.180E+02	0.801E+01	0.130E+02	0.275E+04	0.265E+03	0.109E+03	0.902E+03

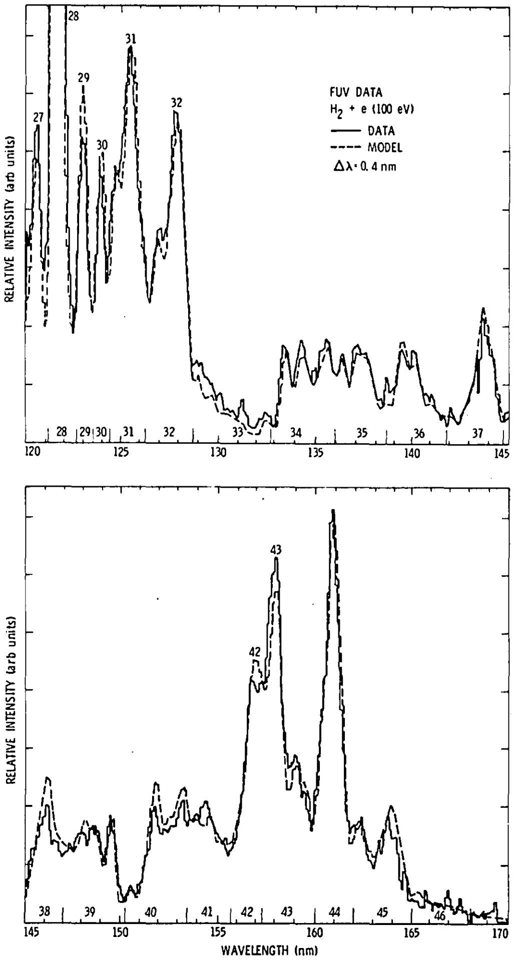

Fig. 7. Laboratory spectrum at 0.4-nm resolution observed at 100 eV and best model fit for the FUV region. The consecutive numbered areas (28–46) used for calibration comparisons are discussed in the text.

lent. Similarly, Fig. 7 shows the experimental and modeled FUV spectrum of H_2 at 0.4-nm resolution. Once again the H_2 model fits the data calibrated with the N_2 molecular branching ratio technique.[18] In this way the experimental data confirm the accuracy for the theoretical data for H_2. The model fits to the calibrated data show a root sum square deviation of <5% in the FUV and 12% in the EUV. We list in Tables III and IV a comparison of the theoretical and experiment fits in forty-six consecutive regions from 77 to 168 nm. In a spectral analysis for calibration purposes it is more accurate to measure areas than peak heights. The areas are chosen to begin and end at minima in the spectra, and each region extends over a wavelength range of ~2.0 nm, a region small enough that changes in calibration are small over the useful range of the spectrometer detector system but large enough to have an adequate SNR. A finer grid can be chosen if a particular wavelength region has a large variation in calibration sensitivity. Intervals 33, 36, and 46 in the FUV are not recommended for calibration use because of poor signal to noise and difficulty in background subtraction. Intervals 2, 6, 7, 22 in the EUV are not recommended for calibration probably due to deficiencies in the model viz D' transition probabilities, which have not been accurately calculated, and affect mainly the 85–90-nm range and intensity perturbations which have not been calculated or measured. Feature 2 is weak and has a less than satisfactory signal to noise.

In our opinion the H_2 technique is superior to the double-monochromator technique because of its basic experimental simplicity. The following advantages are obtained using H_2 calibrated emissions: (1) polarization from rotational bands at 100 eV is negligible (<5%); (2) an additional spectrometer with its extra reflection(s) is eliminated; (3) analysis of e-beam spectra on file can always be updated as models improve.

V. Nitrogen

A complete set of LBH intensity calibration factors $I_{v'v''}$ vs wavelength for the band system is given in Table V. The same table appears in Ref. 15. There are NI features noted in Table V which can blend with the N_2 LBH features depending on instrument resolution. We have shown in Ref. 15 that

$$\sum_{\substack{v'=0 \\ \text{all } v''}}^{6} I_{v'v''} = 0.877. \qquad (6)$$

The Franck Condon factors and transition probabilities are taken from Ref. 34. The summation in Eq. (6) does not result in unity since for $v' > 6$ the vibrational levels of the $a^1\Pi_g$ state predissociate. The $I_{v'v''}$ are accurate only for $\epsilon > 30$ eV due to threshold effects. The LBH cross section peaks near 17 eV. We find 50 eV is an optimum energy for calibration studies based on a trade-off of SNR considerations and stable electron gun operation over extended integration periods (1–3 days). Representative experimental spectra are shown in Ref. 15.

The data set of intensity vs wavelength in Table V can be readily convoluted with any desired slit function for obtaining a reference calibration spectrum. Relative calibration at the wavelengths of the NI multiplets using the relative cross sections in Ref. 15 is most easily obtained at 100 eV. An overplot of two theoretical $N_2(a^1\Pi_g \rightarrow X^1\Sigma_g^+)$ spectra at 0.5-nm resolution is shown in Fig. 8. One spectrum is obtained with triangular and the other spectrum is obtained with a Gaussian transmission function or slit function line shapes. The spectra are virtually identical except for the broadened base associated with a Gaussian transmission function. The sixty-one intense features at 0.5-nm resolution arising from the emission spectrum of the $a^1\Pi_g \rightarrow X^1\Sigma_g^+$ band system are listed in Table VI. A comparison of calibration areas for the particular case $\Delta\lambda = 0.5$ nm with Gaussian and triangular transmission functions is given in Table IV. The areas are chosen to correspond to a wavelength interval of one or more whole bands of ~1.0 nm = 2 × FWHM. The

Table III. EUV Calibration Integrated Intensities from H_2 at 100-eV Electron Impact Energy and 0.5-nm Resolution

Feature No.	peak Theory (nm)	peak Observed (nm)	Wavelength Interval start (nm)	end (nm)	Normalized* Theory	Normalized* Expt'l	Theory Expt'l (% Fit)
1	79.51	79.5	76.8	80.2	---	0.023	---
2	80.60	80.9	80.2	81.4	0.0427	0.039	109
3	81.90	82.0	81.4	83.0	0.0801	0.080	100
4	83.99	84.0	83.0	84.4	0.0875	0.090	97
5	85.38	85.4	84.4	86.0	0.228	0.258	88
6	86.87	86.7	86.0	87.4	0.280	0.252	111
7	87.97	87.9	87.4	88.3	0.191	0.154	124
8	88.67	88.8	88.3	89.6	0.192	0.234	82
9	90.16	90.2	89.6	90.7	0.236	0.239	99
10	91.75	91.8	90.7	92.7	0.646	0.618	104
11	93.05	93.1	92.7	94.0	0.377	0.390	97
12	94.74	94.7	94.0	95.9	0.871	0.851	102
13	96.73	96.6	95.9	98.0	1.255	1.342	94
14	98.72	98.7	98.0	99.8	1.105	1.205	92
15	101.1	101.3	99.8	102.1	1.198	1.298	92
16	102.6	102.7	102.1	104.0	1.526	1.476	103
17	105.4	105.3	104.0	106.1	1.532	1.382	111
18	106.8	106.8	106.1	107.3	0.435	0.441	99
19	109.0	109.0	107.3	109.4	0.902	0.919	98
20	110.0	110.0	109.4	111.0	1.261	1.166	108
21	111.7	111.6	111.0	112.6	1.000	1.00	100
22	113.0	113.0	112.6	113.8	0.251	0.344	75
23	114.6	114.6	113.8	115.2	0.452	0.486	93
24	116.1	116.1	115.2	116.9	1.079	1.175	92
25	117.5	117.5	116.9	118.5	1.136	1.289	88
26	118.9	118.9	118.5	119.6	0.621	0.697	89
27	120.5	120.5	119.6	120.9	0.638		

RMS Difference Model & Experiment = 10.2%

*normalized to unity for Feature No. 21

rotational structure of any vibrational band at 300 K can be calculated. The FWHM of a typical vibrational band due to its rotational structure is 0.05 nm. At the instrumental resolution considered in this calibration paper, Δλ ≥ 0.4 nm, the rotational FWHM is small and does not affect the band shapes displayed.

VI. Helium

The excitation function of the He $(1s^2\,{}^1S - 1snp\,{}^1P^0$, $n = 2,3,4)$ transitions has been established with increasing accuracy over the past few years.[14] Hall *et al.*[35] have separated the cascade and direct excitation components at and above threshold using a detailed collisional model so that emission and electron energy loss experiments can be compared directly. The emission lines appear at 58.43, 53,70, and 52.22 nm. The absolute cross sections have been established by direct measurement and by application to the first Born approximation at high energy.[14] Accurate analytic excitation functions have been established by Shemansky

Table IV. FUV Calibration Integrated Intensities from H_2 at 100-eV Electron Impact Energy and 0.4-nm Resolution

Feature No.	peak Theory (nm)	peak Theory (nm)	Wavelength start (nm)	Interval end (nm)	Area Experiment	Area Theory	Theory Expt'l % Fit
28	121.57	121.6	121.1	122.6	-----	-----	-----
29	122.94	123.0	122.6	123.5	0.519	0.508	97.8
30	123.93	123.9	123.5	124.3	0.427	0.402	106
31	125.3	125.4	124.3	126.4	1.280	1.286	100.4
32	127.91	127.8	126.4	128.8	1.12	1.110	99.1
33	129.01	129.2	128.8	132.9	0.478	0.271	56.6
34	133.59,49.8, 56.8	133.5,4.4, 5.7	132.9	136.0	0.496	0.504	101.6
35	137.17	137.3	136.0	138.6	0.409	0.382	93.3
36	139.56	139.5	138.6	141.9	0.472	0.404	85.5
37	143.64	143.7	141.9	144.7	0.412	0.415	100.7
38	146.23	146.2	144.7	146.9	0.358	0.398	111.2
39	149.52	149.4	146.9	150.3	0.580	0.524	99.0
40	151.81	151.7	150.3	153.4	0.561	0.650	115.8
41	15.44	154.4	153.4	155.6	0.496	0.471	95.0
42	156.88	156.7	155.6	157.4	0.677	0.736	108.7
43	157.88	158.0	157.4	159.9	1.14	1.070	93.8
44	160.87	160.8	159.9	161.9	1.00	1.00	100
45	163.95	163.8	161.9	165.0	0.559	0.577	103.5
46	165.35,67.4	165.1,6.9	165.0	168.0	0.168	0.131	78.0

Av. Fit. 29-46 not 33 = 100.7%

et al.[14] and Hall *et al.*,[35] eliminating the need for interpolation of data. The He transitions are regarded as primary standards because cross sections have been related to intrinsic atomic properties. Care must be taken in the use of the He Rydberg transitions experimentally to account for polarization effects.[36] Energies greater than or equal to 200 eV are recommended, since polarization is <15% for $n = 2,3,4$. For example, the angular variation in intensity for 15% polarization is 5%. The relative intensities of $n = 2,3,4$ are essentially independent of the angular variations due to polarization[36] at 200 eV, since the individual polarizations differ by <5%. Corrections for self-absorption of the lines are generally required.[14] Emission and excitation cross sections at 200 eV are given in Table VII, as derived by Hall *et al.*[35]

In the linear pressure region (~1 × 10^{-6} Torr) a comparison of He (58.43 nm) and H Ly-α calibration signals with equal or known head pressure ratios in the capillary array at 200 eV can be used to fix the 58.4–121.6-nm spectral sensitivity. The present estimates of emission cross section at 200 eV are 5.15×10^{-18} and 8.58×10^{-18} cm^2 for H Ly-α (see Pang *et al.*[13] for references and Table I) and He (58.4 nm),[35] respectively.

VII. Argon

A calibrated EUV spectrum of electron excited Ar at 200 eV is shown in Fig. 9. A detailed analysis and model of the spectrum are in preparation. This allows a calibration in the short-wavelength range of the EUV from 50 to 95 nm. The eleven Ar I and II features are listed in Table VII. Detailed spectroscopic notation can be found in Ref. 37. Features IX and X are Ar I multiplets and are subject to strong self-absorption. These must be corrected for self-absorption or removed from the calibration procedure unless the column abundance criterion in Table VII is met. The remaining features are Ar II. The wavelength intervals are chosen quite large (~3 nm). Thus the relative calibration areas in Table VIII are independent of slit width for $\Delta\lambda < 1.0$ nm. We claim only 35% accuracy with these calibration areas normalized to Feature XI. They are primarily limited in accuracy by the double-

Table V. LBH Relative Intensities vs Wavelength

Band ($v'v''$)	Wavelength (nm)	Theoretical Emission Fraction of Excitation†* cross section $I_{v'v''}$
(0,0)	145.0	0.24732E-02
(0,1)	150.1	0.78524E-02
(0,2)	155.5	0.11490E-01
(0,3)	161.2	0.10294E-01
(0,4)	167.2	0.63432E-02
(0,5)	173.6	0.28342E-02
(0,6)	180.5	0.95700E-03
(0,7)	187.8	0.24539E-03
(0,8)	195.6	0.49077E-04
(0,9)	204.0	0.61346E-04
(1,0)	141.6	0.19461E-01
(1,1)	146.4	0.29275E-01
(1,2)	151.5	0.10867E-01
(1,3)	157.0	0.66877E-04
(1,4)	162.7	0.98643E-02
(1,5)	168.8	0.18274E-01
(1,6)	175.2	0.15181E-01
(1,7)	182.1	0.77911E-02
(1,8)	189.5	0.27921E-02
(1,9)	197.3	0.71892E-03
(1,10)	205.7	0.13375E-03
(1,11)	214.7	0.16720E-04
(2,0)	138.4	0.46412E-01
(2,1)	143.0	0.23809E-01
(2,2)	147.9	0.75344E-03
(2,3)	153.0	0.21498E-01
(2,4)	158.5	0.15068E-01
(2,5)	164.2	0.75344E-04
(2,6)	170.3	0.97947E-02
(2,7)	176.8	0.21247E-01
(2,8)	183.8	0.18057E-01
(2,9)	191.1	0.90413E-02
(2,10)	199.0	0.30389E-02

Continued

monochromator calibration technique in Ref. 21. The relative calibration from 50 to 80 nm is accurate to 25%. The pressure correction to the Ar resonance lines is accurate to 22%. Signal statistics are measured to be 12%. The root sum square uncertainty is 35%.

Outside the threshold energy region polarization of the source radiation is unimportant for H_2 and N_2 due to rotation of the molecule. However, atomic radiation may be polarized. We find the intensities of 92.0 and 93.2 nm of the Ar II emissions were independent of

Table V, continued

Band (v'v"0	Wavelength (nm)	Theoretical Emission Fraction of Excitation cross section $I_{v'v''}^{+*}$
(2,11)	207.4	0.75344E-03
(2,12)	216.5	0.12557E-03
(2,13)	226.2	0.25115E-04
(3,0)	135.4	0.58315E-01
(3,1)	139.8	0.35384E-02
(3,2)	144.4	0.19694E-01
(3,3)	149.3	0.16046E-01
(3,4)	154.5	0.87774E-03
(3,5)	160.0	0.18241E-01
(3,6)	165.8	0.10697E-01
(3,7)	171.9	0.82284E-04
(3,8)	178.5	0.11438E-01
(3,9)	185.4	0.19859E-01
(3,10)	192.8	0.14839E-01
(3,11)	200.7	0.66379E-02
(3,12)	209.2	0.20024E-02
(3,13)	218.2	0.43887E-03
(3,14)	227.9	0.54859E-04
(4,0)	132.5	0.48539E-01
(4,1)	136.8	0.17082E-02
(4,2)	141.2	0.23916E-01
(4,3)	145.9	0.97615E-04
(4,4)	150.8	0.15789E-01
(4,5)	156.0	0.64426E-02
(4,6)	161.6	0.30993E-02
(4,7)	167.4	0.14227E-01
(4,8)	173.6	0.42707E-02
(4,9)	180.1	0.14398E-02
(4,10)	187.1	0.11958E-01
(4,11)	194.5	0.15033E-01
(4,12)	202.5	0.91758E-02
(4,13)	210.9	0.33897E-02
(4,14)	220.0	0.90294E-03
(4,15)	229.7	0.17083E-03
(4,16)	240.2	0.24404E-04
(5,0)	129.9	0.30414E-01
(5,1)	133.9	0.10572E-01

Continued

angle measured with respect to the electron beam axis at 200 eV to +5%. The polarization of the Ar I resonance lines has been measured to be close to zero at 200 eV for the 104.8- and 106.7-nm emissions.[38] We assume that the other resonance lines at wavelengths between 80.0 and 90.0 nm in Table VII have small polarization at 200 eV. The argon spectrum in Fig. 9 was measured at 90° emission angle with respect to the electron-beam axis.

Table V, continued

Band (v'v")	Wavelength (nm)	Theoretical Emission Fraction of Excitation+* cross section $I_{v'v''}$
(5,2)	138.2	0.95717E-02
(5,3)	142.7	0.64001E-02
(5,4)	147.4	0.93641E-02
(5,5)	152.3	0.14159E-02
(5,6)	157.6	0.10742E-01
(5,7)	163.1	0.77405E-03
(5,8)	169.0	0.56071E-02
(5,9)	175.2	0.81558E-02
(5,10)	181.8	0.45310E-03
(5,11)	188.8	0.36248E-02
(5,12)	196.3	0.10119E-01
(5,13)	204.2	0.90053E-02
(5,14)	212.7	0.43610E-02
(5,15)	221.8	0.13593E-02
(5,16)	231.5	0.30207E-03
(5,17)	242.0	0.37758E-04
(6,0)	127.3	0.15369E-01
(6,1)	131.2	0.14240E-01
(6,2)	135.3	0.69560E-03
(6,3)	139.6	0.10053E-01
(6,4)	144.1	0.31499E-03
(6,5)	148.9	0.72185E-02
(6,6)	153.9	0.13518E-02
(6,7)	159.2	0.39505E-02
(6,8)	164.8	0.43312E-02
(6,9)	170.7	0.26249E-03
(6,10)	176.9	0.54205E-02
(6,11)	183.5	0.27299E-02
(6,12)	190.6	0.21000E-03
(6,13)	198.1	0.45805E-02
(6,14)	206.0	0.66017E-02
(6,15)	214.5	0.42393E-02
(6,16)	223.6	0.16275E-02
(6,17)	233.3	0.40687E-03
(6,18)	243.8	0.65623E-04
(6,19)	255.0	0.13125E-04

Continued

As an aside, heavier rare gases such as Xe and Kr can be used with a supersonic gas jet for cooling the gas to near absolute zero instead of a capillary array with a gas at room temperature to produce extremely narrow resonance lines, $\lambda/(\Delta\lambda) \cong 10^6$ in the VUV. This narrow line source is useful for measuring spectral line transmission functions for high-resolution VUV spectrometers.

Table V, continued

Summary Total

$q_{00} = 0.04308$

$q_{10} = 0.1155$

$q_{20} = 0.1707$

$q_{30} = 0.1832$

$q_{40} = 0.1600$

$q_{50} = 0.1217$

$q_{60} = 0.08296$

$$\sum_{\substack{v'=0\\ \text{All } v'}}^{6} f_{v'v''} = \sum_{v'=0}^{6} q_{v'0} = 0.8771$$

*at the high energy limit.

+Important NI multiplets blending with LBH features and effecting experimental $I_{v'v''}$

Wavelength (nm)	Transition
116.40	$^2D^0-^2D$
117.69	$^2D^0-^2P$
119.99	$^4S^0-^4P$
124.33	$^2D^0-^2D$
131.07	$^2P^0-^2D$
131.95	$^2P^0-^2P$
132.70	$^2P^0-^2P$
141.19	$^2P^0-^2D$
149.33	$^2D^0-^2P$
174.36	$^2P^0-^2P$

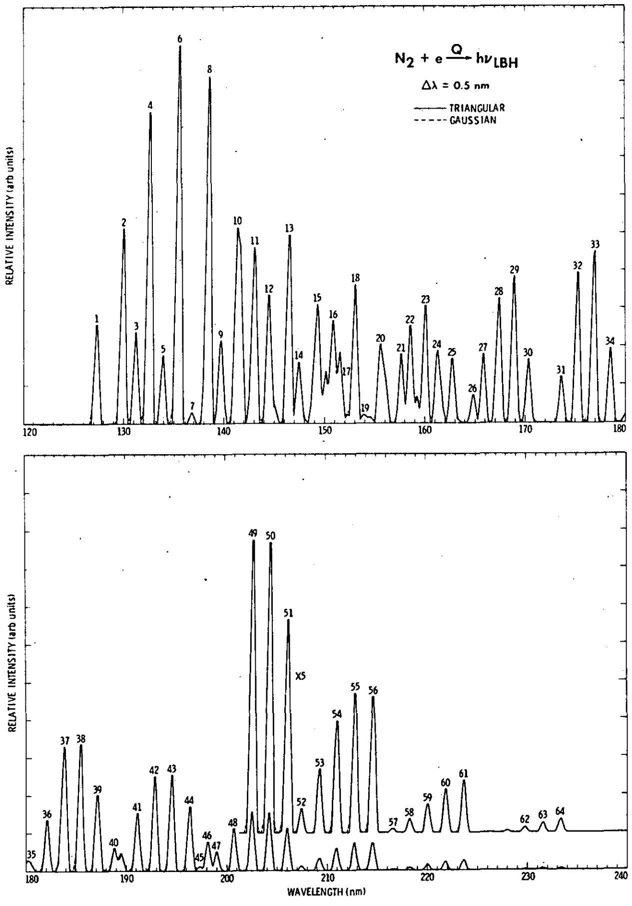

Fig. 8. Synthetic spectra of N_2 for $\epsilon > 30$ eV without NI lines[15] for $\Delta\lambda = 0.5$-nm FWHM and triangular and Gaussian slit functions.

VIII. Galileo Calibration

The ultraviolet spectrometer (UVS) for the Galileo spacecraft was recently calibrated at the University of Colorado's Laboratory for Atmospheric and Space Physics using the electron-beam source described above. These results were compared with independent measurements of the UVS sensitivity derived from an irradiance standard and from a laboratory photomultiplier tube which was calibrated using a National Bureau of Standards photodiode.

The Galileo UVS consists of a Cassegrain telescope with a 14-cm^2 unobscured aperture feeding a 125-mm focal length Ebert Fastie monochromator. Three pulse counting photomultiplier tubes, located in the focal plane of the monochromator, measure a spectrum in the 110–430-nm wavelength range. The photocathode for each detector is selected on the basis of its wavelength response; the *G* channel detector has a cesium iodide photocathode for a solar blind response (110–180 nm); the *F* channel detector has a cesium teluride photocathode (160–320 nm); and the *N* channel detector has a cesium potassium antimony photocathode (280–430 nm). Exit slits located at the focal plane provide a triangular bandpass of 0.7-nm FWHM for the *G* channel and 1.3-nm FWHM for the *F* and *N* channels.

Absolute photometric sensitivity for both the *G* and *F* channels was measured by placing the UVS in a collimated beam provided by an auxiliary telescope fed by a monochromator equipped with a deuterium discharge lamp. A pulse counting photomultiplier tube calibrated with a National Bureau of Standards photodiode was used to measure the photon flux in the beam incident on the UVS telescope aperture. Computer-controlled stepper motors drove a scan platform on which the photomultiplier was mounted so that the input beam could be completely mapped. A beam splitter positioned just after the auxiliary monochromator directed 5% of the light from the beam to a second photomultiplier to monitor lamp drift during calibration observations and beam mapping. This arrangement provided a direct measurement of the UVS efficiency in units of counts per incident photon as a function of wavelength for the 120–300-nm wavelength range. The results can be expressed in counts/s/kR (a kilorayleigh is 10^9 photons/cm^2 s emitted over 4π sr) by incorporating the field of view of the UVS monochromator entrance slit is (0.1 × by 1.4° for the *G* and *N* channel and 0.1 × 0.4° for the *F* channel). Additional measurements of the *F* and *N* channel sensitivity were made using a freshly prepared barium sulfate scattering screen and a deuterium lamp with a spectral irradiance, which is traceable to a National Bureau of Standards calibration.[5,8,9] Scattering screen results can be directly expressed in counts per kilorayleigh.

Spectra of molecular nitrogen in all three UVS channels and of molecular hydrogen in the *G* channel were obtained using the electron-beam source described above (Fig. 1). The UVS and electron-beam source were mounted 75 cm apart inside a large vacuum tank, which was operated typically at a pressure of 10^{-5} Torr. Lamp head pressure was 1–10 Torr during all the calibration observations. Several data taking trials were made for each channel. Relative molecular band intensities were observed to be constant from run to run despite small changes in lamp head pressure, electron gun current, and UVS viewing geometry. On the other hand, the ratio of atomic features to molecular features was seen to be a function of viewing geometry since the excited atomic states have short lifetimes relative to the excited molecular states and radiate almost entirely within the collision region. For this reason it was necessary to exclude molecular bands which were blended with atomic features from the calibration data.

Figure 10 shows a comparison of the *G* channel spectrum of H_2 (solid curve) taken with an electron energy of 100 eV and a synthetic spectrum convolved with a triangular transmission function, which had a 0.7-nm FWHM (dotted line). The strong feature at 121.6 nm is due to hydrogen Lyman-α emission and is the only atomic feature in this wavelength range. For convenience the two spectra have been normalized near 160 nm. A relative spectral sensitivity calibration was

Table VI. N_2 LBH FUV Calibration Factors at $\epsilon > 50$-eV Electron Impact Energy and 0.5-nm Resolution

Feature #	peak (nm)	Wavelength start* (nm)	Wavelength end* (nm)	Calibration $I_{v'v''}$ Triangular	Area $I_{v'v''}$ Gaussian
1	127.3	126.9	127.8	0.0154	
		126.4	128.4		0.0154
2	129.9	129.4	130.4	.0304	
		128.4	130.6		.0304
3	131.2	130.7	131.7	.0142	
		130.6	131.8		.0142
4	132.5	132.0	133.0	.0485	
		131.8	133.3		.0486
5	133.9	133.4	134.4	.0106	
		133.3	134.6		.0105
6	135.3	134.8	135.9	.0590	
		134.6	136.3		.0590
7	136.8	136.3	137.3	.00171	
		136.3	137.5		.00169
8	138.4	137.7	138.9	.0560	
		137.5	139.1		.0561
9	139.6	139.1	140.3	.0136	
		139.1	140.5		.0135
10	141.8	140.7	142.1	.0436	
		140.5	142.3		.0436
11	143.0	142.2	143.5	.0302	
		142.3	143.7		.0300
12	144.4	143.6	145.6	.0225	
		143.7	145.6		.0225
13	146.4	145.6	147.0	.0296	
		145.6	147.0		.0296
14	147.5	147.0	148.4	.00993	
		147.0	149.5		0.0103

Continued

Table VI, continued

Feature #	peak (nm)	Wavelength start* (nm)	Wavelength end* (nm)	Calibration $I_{v'v''}$ Triangular	Area $I_{v'v''}$ Gaussian
15	149.2	148.4	149.9	.0247	
		148.5	149.8		.0235
16	150.8	149.9	152.1	.0333	
		149.8	152.1		.0342
17	152.3	152.1	152.6	.00148	
		152.1	152.6		.00177
18	153.0	152.6	153.6	.0213	
		152.6	153.7		.0211
19	153.9	153.6	154.4	.00153	
		153.7	154.3		.00124
20	155.5	154.4	156.5	.0185	
		154.3	156.8		.0187
21	157.6	156.5	158.1	.0111	
		156.8	158.1		.0117
22	158.5	158.1	159.5	.0184	
		158.1	159.5		.0185
23	160.0	159.5	160.5	.0186	
		159.5	160.7		.0185
24	161.2	160.7	162.1	.0134	
		160.7	162.1		.0133
25	162.7	162.2	163.6	.0106	
		162.1	163.8		.0106
26	164.8	163.7	165.3	.00441	
		163.8	165.3		.00447
27	165.8	165.3	166.3	.0107	
		165.3	166.6		.0106
28	167.4	166.7	167.9	.0206	
		166.6	168.1		.0206
29	168.9	168.3	169.5	.0239	
		168.1	169.7		.0239

Continued

Table VI, continued

Feature #	peak (nm)	Wavelength start* (nm)	Wavelength end* (nm)	Calibration $I_{v'v''}$ Triangular	Area $I_{v'v''}$ Gaussian
30	170.6	169.8	171.2	.0101	
		169.7	171.4		.0100
31	173.6	173.1	174.1	.00710	
		172.9	174.4		.00710
32	175.2	174.7	175.7	.0233	
		174.4	176.1		.0234
33	176.2	176.3	177.4	.0267	
		176.1	177.7		.0267
34	178.5	178.0	179.0	.0114	
		177.7	179.4		.0114
35	180.1	179.6	181.0	.00239	
		179.4	181.2		.00240
36	182.1	181.3	182.6	.00825	
		181.2	182.9		.00825
37	183.8	183.0	184.3	.0208	
		182.9	184.6		.0208
38	185.4	184.9	185.9	.0199	
		184.6	186.3		.0199
39	187.1	186.6	188.3	.0122	
		186.3	188.3		.0122
40	189.5	188.3	190.0	.00641	
		188.3	190.2		.00638
41	191.1	190.1	191.5	.00907	
		190.2	192.0		.00925
42	192.8	192.3	193.3	.0148	
		192.0	193.7		.0148
43	194.5	194.0	195.0	.0150	
		193.7	195.4		.0150
44	196.3	195.1	196.9	.0102	
		195.4	197.0		.0102

Continued

Table VI, continued

Feature #	peak (nm)	Wavelength start* (nm)	Wavelength end* (nm)	Calibration $I_{v'v''}$ Triangular	Area $I_{v'v''}$ Gaussian
45	197.3	196.9	197.6	.000650	
		197.0	197.6		.000660
46	198.1	197.6	198.6	.00469	
		197.6	198.6		.00464
47	199.0	198.6	199.5	.00298	
		198.6	199.9		.00299
48	200.7	200.2	201.2	.00664	
		199.9	201.6		.00663
49	202.5	202.1	203.0	.00900	
		201.6	203.4		.00918
50	204.2	203.5	204.7	.00906	
		203.4	205.1		.00907
51	205.9	205.2	206.5	.00674	
		205.1	206.8		.00673
52	207.4	206.9	207.9	.000750	
		206.8	208.2		.000760
53	209.2	208.7	209.7	.00200	
		208.5	210.0		.00200
54	210.9	210.4	211.4	.00349	
		210.1	211.8		.00349
55	212.7	212.2	213.2	.00437	
		211.8	213.6		.00436
56	214.6	214.0	215.2	.00425	
		213.7	215.6		.00425
57	216.5	216.0	217.0	.000130	
		215.6	217.4		.000130
58	218.2	217.7	218.7	.000440	
		217.4	219.0		.000440
59	220.0	219.5	220.5	.000900	
		219.0	220.9		.000900

Continued

Table VI, continued

Feature #	peak (nm)	Wavelength start* (nm)	Wavelength end* (nm)	Calibration $I_{v'v''}$ Triangular	Area $I_{v'v''}$ Gaussian
60	221.8	221.3	222.3	.00136	
		220.9	222.7		.00136
61	223.6	223.1	224.1	.00163	
		222.7	224.6		.00163
				Total 1100 - 2300 =	
				0.874	0.875

*Theoretical wavelength intervals without rotational structure

established by comparing the strengths of the molecular features band by band and is shown in Fig. 11. In that figure the solid line is the UVS absolute sensitivity calibration based on the discharge lamp and calibrated photomultiplier; the dotted and dashed curves are the relative calibrations for H_2 at 100 eV and N_2 at 50 eV, respectively, derived from the electron-beam source. The N_2 calibration spans the 130–180-nm range; the H_2 calibration spans the 115–170-nm range allowing the UVS sensitivity measurements to be extended to shorter wavelengths than possible using the calibrated photomultiplier. Figure 12 compares the results for the F channel detector. The solid and dashed lines are the absolute calibration measurements derived from the deuterium lamp and the calibrated photomultiplier, respectively. The dotted line is the relative calibration based on the 50-eV N_2 spectrum from the electron lamp for the 170–223-nm range.

IX. Discussion

We have developed a simple compact laboratory source of UV radiation in which relative emission intensity as a function of wavelength depends directly on the fundamental constants (transition probabilities and collision strengths) for molecular or atomic systems. Using this source, laboratory standard electron impact VUV spectra have been measured and synthetic models developed for (1) H_2 Rydberg series, H Ly-α and H Ly-β, (2) the $N_2(a^1\Pi_g \rightarrow X^1\Sigma_g^+)$ band system, and (3) the $n\ ^1P^0$, $n = 2,3,4$ Rydberg series of He. These laboratory measurements together with a spectroscopic model allow the VUV spectrum from H_2 and N_2 to serve as a relative intensity calibration standard. The 10% accuracy of the model fit to the two sets of data appears to be sufficient for it to serve as an intensity calibration standard for VUV instruments in the 80–230-nm wavelength range. The ~3% accuracy of a synchrotron calibration remains superior. A somewhat larger uncertainty of 20% is given for the range from 80 to 90 nm. Account must be taken of optical depth effects for foreground abundances of $>3 \times 10^{12}$ cm^2 for H_2 in the EUV region (90–105 nm). The He $n = 2$, 3, and 4 Rydberg series from 52 to 58.4 nm have been established as primary standards over the entire energy range from threshold. A calibrated VUV spectrum of Ar has been obtained for service as an intensity standard over the wavelength range of 50–95 nm that complements the H_2 results.

We suggest that the sources described here provide a convenient primary standard for use in the laboratory. This is a practical alternative to transporting the VUV space flight or laboratory instrumentation to the regional synchrotron source.

This work was supported by the Air Force Office of Scientific Research (AFOSR), the Aeronomy Program of the National Science Foundation, and NASA Planetary Atmospheres and Astronomy/Relativity Program Offices under contract NAS7-100 to the Jet Propulsion Laboratory, California Institute of Technology, Pasadena, CA 91109, NAGW-106, to the University of Southern California, Los Angeles, CA 90089 and NAGW-649 to the University of Arizona, Tucson, AZ 85721. G. K. James acknowledges receipt of an NRC Resident Research Associateship.

Table VII. Helium Cross Sections at 200 eV[*]

Transition	λ (nm)	Direct Cross Section (10^{-18} cm^2)	Cascade Emission Cross Section[+] (10^{-18} cm^2)	Total Emission Cross Section[+] (10^{-18} cm^2)	Branching Ratio
$2\ {}^1P^o \rightarrow 1\ {}^1S$	58.43	8.13	0.46	8.58	0.999
$3\ {}^1P^o \rightarrow 1\ {}^1S$	53.70	2.02	0.06	2.03	0.976
$4\ {}^1P^o \rightarrow 1\ {}^1S$	52.22	0.84	0.02	0.83	0.965

[*] Hall et al., Ref. 35.

[+] To obtain total excited state cross section divide by branching ratio.

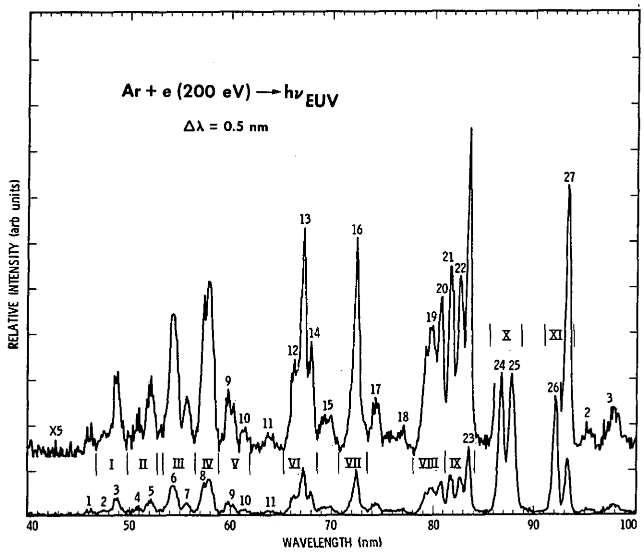

Fig. 9. Optically thin electron impact spectrum of Ar at 200 eV and Δλ = 0.5-nm FWHM. Corrections of ~10% have been made for the Ar I lines between 80 and 95 nm. The actual experimental spectrum was obtained at a pressure of 6 × 10^{-7} Torr and over a 25-cm path length.

Appendix A: Theoretical Investigation of Axial Magnetic Field

For the theoretical investigation of the axial magnetic field from a scalar potential we consider four magnets of length $2d$ placed parallel to the z axis at the four corners of a square centered on the origin with a diagonal of length $2l$ (Fig. 13). The magnets all have the same polarity, and their centers lie in the x-y plane.

Assuming equal pole strengths M, the magnetic potential of this configuration is

$$\begin{aligned} U_m = M[&r^{-1}(l,0,d) - r^{-1}(-l,0,d) + r^{-1}(0,-l,-d) \\ &-r^{-1}(0,-l,d) + r^{-1}(l,0,-d) - r^{-1}(l,0,d) \\ &+ r^{-1}(0,l,-d) - r^{-1}(0,l,d)], \end{aligned} \tag{A1}$$

where we have written

$$r^n(a,b,c) = [(x + a)^2 + (y + b)^2 + (z + c)^2]^{n/2}. \tag{A2}$$

The resultant magnetic field is calculated from the relationship

$$\mathbf{B} = \nabla U_m. \tag{A3}$$

From these equations $\mathbf{B}$ can be written in component form

$$\begin{aligned} B_x = M\{&(x - l)[r^{-3}(-l,0,d) - r^{-3}(-l,0,-d)] \\ &+ (x + l)[r^{-3}(l,0,d)] - r^{-3}(l,0,-d)] + x[r^{-3}(0,-l,d) \\ &- r^{-3}(0,-l,-d)] + x[r^{-3}(0,l,d) - r^{-3}(0,l,-d)]\}, \end{aligned} \tag{A4}$$

$$\begin{aligned} B_y = M\{&(y - l)[r^{-3}(0,-l,d) - r^{-3}(0,-l,-d)] \\ &+ (y + l)[r^{-3}(0,l,d) - r^{-3}(0,l,-d)] + y[r^{-3}(-l,0,d) \\ &- r^{-3}(-l,0,-d)] + y[r^{-3}(l,0,d) - r^{-3}(l,0,-d)]\}, \end{aligned} \tag{A5}$$

Table VIII. Low-Pressure Electron Impact EUV Calibration Relative Intensities of Argon at 200 eV and 0.5-nm Resolution*

Interval #	Wavelength Interval (nm)	Relative Calibration Area
I	46.8-49.8	0.178
II	49.8-52.8	0.193
III	53.4-56.4	0.380
IV	56.4-58.9	0.432
V	58.9-62.1	0.159
VI	65.3-68.6	0.533
VII	70.8-73.6	0.333
VIII	78.1-81.2	0.510
IX	81.2-84.2	0.814
X	85.5-89.4	1.941
XI	91.1-93.9	1.000

*Relative uncertainty 35%. Foreground abundances for calibration intensities given in interval IX and X must be measured with abundances < 2 x 10^{11} cm^{-2} since IX and X are Ar I resonance lines. Features I-VII and XI are independent of pressure since they are Ar II lines.

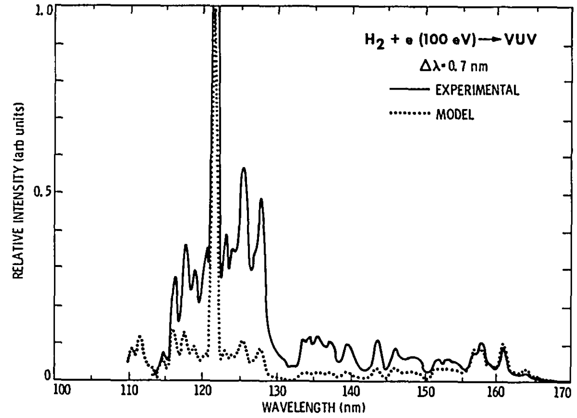

Fig. 10. Comparison of $H_2 + e$ (100-eV) spectrum (solid line) measured by uncalibrated Galileo UVS with a calibrated synthetic spectrum of 0.7-nm FWHM triangular transmission function (dotted line). The spectra have been normalized at 160 nm.

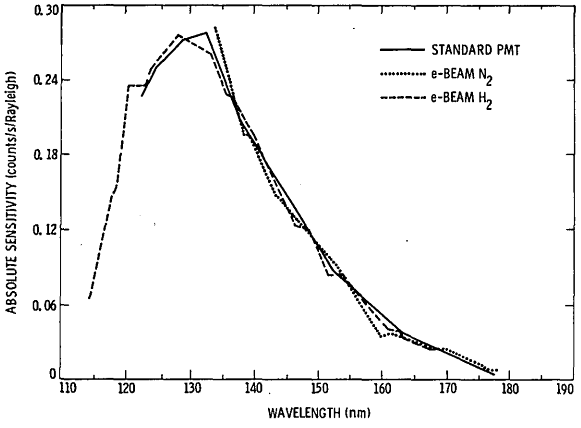

Fig. 11. Galileo UVS absolute sensitivity comparison based on: (1) dotted line—$H_2 + e$ (100 eV); (2) dashed line—$N_2 + e$ (50 eV); (3) solid line—calibrated photomultiplier and discharge lamp. The electron-beam relative calibration was normalized to the calibrated photomultiplier calibration at 170 nm.

$$
\begin{aligned}
B_z = M\{(z + d)[r^{-3}(-l,0,d) + r^{-3}(l,0,d) + r^{-3}(0,-l,d) \\
+ r^{-3}(0,l,d)] - (z - d)[r^{-3}(-l,0,-d) \qquad \text{(A6)} \\
+ r^{-3}(l,0,-d) + r^{-3}(0,-l,-d) + r^{-3}(0,l,-d)]\}.
\end{aligned}
$$

Close to the z axis, the magnetic field lines are confined to planes containing the z axis. These planes can be defined by their angle to the x axis ϕ. The lines of force are then generated by

$$\frac{d\rho}{dz} = (B_x \cos\phi + B_y \sin\phi)/B_z, \qquad \text{(A7)}$$

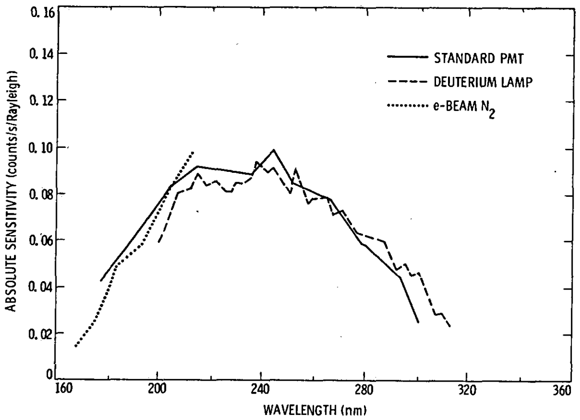

Fig. 12. Galileo UVS absolute sensitivity comparison based on: (1) dotted line—$N_2 + e$ (50 eV); (2) solid line—calibrated photomultiplier; (3) dashed line—deuterium lamp. The electron-beam relative calibration was normalized to the calibrated photomultiplier at 200 nm.

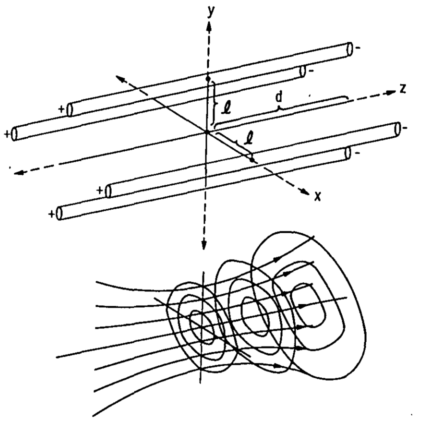

Fig. 13. Magnetic field lines and equipotential lines from a magnetic quadrupole composed of four equal strength ideal for magnets.

where $\rho = (x^2 + y^2)^{1/2}$. For fixed z, lines of equipotential are given by

$$\frac{dy}{dx} = -\frac{B_x}{B_y}\,. \tag{A8}$$

These two equations were integrated numerically, and typical solutions are plotted in Fig. 13. As seen in this figure there is a slight squaring of the equipotential lines. This reflects the cubic symmetry of the system. This effect becomes negligible near the z axis where the lines of force approximate those of a solenoid. The field strength at the origin is

$$H = \frac{8Md}{(l^2 + d^2)^{3/2}}\,. \tag{A9}$$

It should be noted that outside the magnet housing the far field looks like that of a single magnet of pole strength 4M. In this regard, our configuration is significantly different from that of a solenoid where the far field drops off more rapidly.

In practice the magnetic field of the electromagnet conforms more closely to the ideal bar magnet compared with a permanent magnet. The spurious fringe fields near the end of the permanent magnet limit the effective collimation length of the electron beam to 15 cm or about one-third of the length of the bar magnet, whereas the electromagnet provides effective collimation over twice that length. A comparison of the two quadrupole magnetic fields along with that of an electromagnet solenoid with an annulus removed at center for viewing is shown in Fig. 2.

We describe the quadrupole electromagnet in a little more detail due to its inherently more uniform magnetic field. The wire used in the four solenoids composing the electromagnet was 20 gauge aluminum wire with aluminum oxide insulation. The aluminum oxide insulation has excellent vacuum properties in operation due to its minimal outgassing.[39] With a 1.27-cm (0.5-in.) diam soft core iron, turn densities of 1.7×10^4 turns/m are achieved which can yield a maximum of 200-G magnetic field at the center of the magnetic yolk before saturation of the core near 1.25 A. Adequate thermal conductors to shunt away electrical heat from the source are recommended.

We conclude that a simple arrangement of four cylindrical electromagnets, as described in this paper, can be employed to build a magnetically collimated electron gun for the study of electron atom/molecule collision processes.

References

1. J. M. Bridges and W. R. Ott, "Vacuum Ultraviolet Radiometry. 3: The Argon Mini-arc as a New Secondary Standard of Spectral Radiance," Appl. Opt. **16**, 367 (1977).
2. J. Z. Klose, J. M. Bridges, and W. R. Ott, "Radiometric Standards in the Vacuum Ultraviolet," Natl. Bur. Stand. 250-3 U.S. Spec. Publ. (1987), Chaps. 2–4.
3. A. McPherson, N. Rouze, W. B. Westerveld, and J. S. Risley, "Calibration of a VUV Spectrometer Detector System Using Synchroton Radiation," Appl. Opt. **25**, 298 (1986).
4. P. J. Key and R. C. Preston, "Vacuum Ultraviolet Radiation Scales: An Accurate Comparison Between Plasma Blackbody Lines and Synchrotron Radiation," Appl. Opt. **16**, 2477 (1977).
5. R. D. Saunders, W. R. Ott, and J. M. Bridges, "Spectral Irradiance Standard for the Ultraviolet: the Deuterium Lamp," Appl. Opt. **17**, 593 (1978).
6. D. H. Nettleton and R. C. Preston, "Deuterium Lamp Based Monochromator Calibration Extended Down to 115 nm," Appl. Opt. **20**, 1274 (1981).
7. K. Behringer and P. Thoma, "VUV Radiometry Below 100 nm: the High-Power Hydrogen Arc as a Standard Source of Continuum Radiation Between 53 nm and 92 nm," Appl. Opt, **18**, 2586 (1979).
8. W. R. Ott, L. R. Canfield, S. C. Ebner, L. R. Hughey, and R. P. Madden, "XUV Radiometric Standards at NBS," Proc. Soc. Photo-Opt. Instrum. Eng. **689**, 178 (1986).
9. W. R. Ott, "NBS Ultraviolet Radiometric Standards," Natl. Bur. Stand. U.S. Spec. Publ. **456**, 107 (1976); G. L. Weissler and S. K. Srivastava, "A Wall-Stabilized Doubled Arc as a Standard Source in the Vacuum Ultraviolet," in *Space Optics*, ISBN 0-309-02144-8 (National Academy of Sciences, Washington, DC, (1974), p. 772.
10. L. R. Canfield, R. G. Johnston, and R. P. Madden, "NBS Detector Standards for the Far UV," Appl. Opt. **12**, 1611 (1973).

11. R. McAdams and S. K. Srivastava, "Electron-Photon Coincidence Technique for the Absolute Calibration of VUV Detectors," Appl. Opt. **22**, 1551 (1983); see also S. K. Srivastava, "Means and Method for Calibrating a Photon Detector Utilizing Electron-Photon Coincidence Technique," U.S. Patent 4,629,937.
12. J. M. Ajello, "Emission Cross Sections of N_2 in the Vacuum Ultraviolet by Electron Impact," J. Chem. Phys. **53**, 1156 (1970); M. J. Mumma and E. C. Zipf, "Calibration of Vacuum Ultraviolet Monochromators by the Molecular Branching Ratio Technique," J. Opt. Soc. Am. **61**, 83 (1971); M. J. Mumma, "Molecular Branching Ratio Method for Intensity Calibration of Optical Systems in the Vacuum Ultraviolet," J. Opt. Soc. Am. **62**, 1459 (1972).
13. D. E. Shemansky, J. M. Ajello, and D. T. Hall, "Electron Excitation of H_2: Rydberg Band Systems and the Benchmark Dissociative Cross Section of H Lyα," Astrophys. J. **296**, 765 (1985); and K. D. Pang, J. M. Ajello, B. Franklin, and D. Shemansky, "Electron Impact Excitation Cross Section Studies of Methane and Acetylene," J. Chem. Phys. **86**, 2750 (1987).
14. D. E. Shemansky, J. M. Ajello, D. T. Hall, and B. Franklin, "Vacuum Ultraviolet Studies of Electron Impact of Helium: Excitation of He(n^1P^0) Rydberg Series and Ionization Excitation of He$^+$(nl) Rydberg Series," Astrophys. J. **296**, 774 (1985); F. G. Donaldson, M. A. Hender, and J. W. McConkey, "Vacuum Ultraviolet Measurements of the Electron Impact Excitation of Helium," J. Phys. B: Atom. Mol. Phys. **5**, 1192 (1972); W. B. Westerveld, H. G. M. Heideman, and J. Van Eck, "Electron Impact Excitation of $1^1S \rightarrow 2^1P$ and $1^1S \rightarrow 3^1P$ of Helium: Excitation Cross Sections and Polarization Fractions Obtained from XUV Radiation," J. Phys. B: At. Mol. Phys. **12**, 115 (1979).
15. J. M. Ajello and D. E. Shemansky, "A Re-examination of Important N_2 Cross Sections by Electron Impact with Application to the Dayglow: The Lyman-Birge-Hopfield Band System and NI (119.99 nm)," J. Geophys. Res. **90**, 9845 (1985).
16. J. F. M. Aarts, F. J. de Heer, B. F. J. Kuyken, F. W. Saris, L. Vriens, and D. A. Vroom, "New Developments for the Absolute Calibration of Light Intensities in the Far Ultraviolet," Physics **41**, 209 (1969); J. F. M. Aarts and F. J. de Heer, "Extension of the Branching Ratio Method for Intensity Calibration Between 1500 and 2600 A," J. Opt. Soc. Am. **58**, 1666 (1968).
17. J. W. McConkey, "Intensity Calibration Using Molecular Bands Excited by Controlled Electron Impact," J. Opt. Soc. Am. **59**, 110 (1969).
18. J. M. Ajello, S. K. Srivastava, and Y. L. Yung, "Laboratory Studies of UV Emissions of H_2 by Electron Impact. The Werner and Lyman Band Systems," Phys. Rev. A **25**, 2485 (1982).
19. D. J. McEwen, "Intensity Measurements of the Lyman- Birge-Hopfield System of Nitrogen," Ph.D. Thesis, U. Western Ontario (1965).
20. J. R. Pierce, *Theory and Design of Electron Beams* (van Nostrand, New York, 1954).
21. J. M. Ajello, D. Shemansky, T. L. Kwok, and Y. L. Yung, "Studies of Extreme Ultraviolet Emission from Rydberg Series of H_2 by Electron Impact," Phys. Rev. A **29**, 636 (1984).
22. J. M. Ajello and B. Franklin, "A Study of the Extreme Ultraviolet Spectrum of O_2 by Electron Impact," J. Chem. Phys. **82**, 2519 (1985).
23. P. O. Taylor, K. T. Dolder, W. E. Kauppila, and G. H. Dunn, "Measurement of Spiraling in a Magnetically Confined Electron Beam for Use in Collision Studies," Rev. Sci. Instrum. **45**, 538 (1974).
24. J. A. Simpson and C. E. Kuyatt, "Design of Low Voltage Electron Guns," Rev. Sci. Instrum. **34**, 265 (1963).
25. W. C. Tam and S. F. Wong, "Magnetically Collimated Electron Impact Spectrometer," Rev. Sci. Instrum. **50**, 302 (1979).
26. R. E. Fox, W. M. Hickman, D. J. Grove, and T. Kjeldass, "Ionization Potentials and Probabilities Using a Mass Spectrometer," Phys. Rev. **84**, 859 (1951).
27. R. T. Brinkmann and S. Trajmar, "Effective Path Length Corrections in Beam-Beam Scattering Experiments," J. Phys. E **14**, 245 (1981).
28. J. A. R. Samson, *Techniques of Vacuum Ultraviolet Spectroscopy* (Wiley, New York, 1967), Chap. 8.
29. A. C. Allison and A. Dalgarno, "Band Oscillator Strengths and Transition Probabilities for the Lyman and Werner Systems of H_2, HD and D_2," At. Data **1**, 289 (1970); H. Schmoranzer, J. Imschweiler, and T. Noll, "Radiative Lifetimes of Selectively Excited Rotational Lebvels of the $B2p^1\Sigma_g^+$ and $C2p^1\Pi_u$ States of H_2," in *Ninth International Conference on Atomic Physics*, Seattle, WA (July 1984), p. A26.
30. M. Glass Maujean, "Transition Probabilities for the D and B′ Vibrational Levels to the X Vibrational Levels and Continuum of H_2," At. Data Nucl. Data Tables **30**, 301 (1984); T. L. Kwok, A. Dalgarno, and A. Posen, "Transition Probabilities of the $B'^1\Sigma_u^+ \rightarrow X^1\Sigma_g^+$ System of Molecular Hydrogen," Phys. Rev. A **32**, 646 (1985).
31. P. M. Guyon, J. Breton, and M. Glass Maujean, "Predissociation of the $^1\Pi_u^+$ States of H_2: Measurement of the Various Dissociation Yields," Chem. Phys. Lett. **68**, 14 (1979); M. Glass Maujean, J. Breton, and P. M. Guyon, "High Resolution Study of Photoabsorption Phododissociation and Fluorescence in H_2," Z. Phys. D **5**, 189 (1987).
32. I. Dabrowski, "The Lyman and Werner Bands of H_2," Can. J. Phys. **62**, 1639 (1985); T. Namioka, "Absorption Spectra of H_2 in the Vacuum Ultraviolet Region. I. The Lyman and the Werner Bands," J. Chem. Phys. **40**, 3154 (1964); A. Monfils, "The Absorption Spectra of the Molecules of H_2, HD, and D_2 Part VI. Rotational Analysis of the B′, B″, D, D′, and D″ States," J. Mol. Spectrosc. **15**, 265 (1965).
33. H. Abgrall, F. Launary, E. Roueff, and J.-Y. Roncin, "Effect of Rotational Coupling on Emission Probabilities of Lyman and Werner Band Systems of the Vacuum Ultraviolet Spectrum of H_2," J. Chem. Phys. **87**, 2036 (1987).
34. A. Lofthus and P. H. Krupenie, "The Spectrum of Molecular Nitrogen," J. Chem. Ref. Data **6**, 113 (1977); D. E. Shemansky, "N_2 Lyman-Birge-Hopfield System," J. Chem. Phys. **51**, 5487 (1969).
35. D. T. Hall, D. E. Shemansky, and J. M. Ajello, "Helium in Collisional Equilibrium with an Electron Gas," Bull. Am. Astron. Soc. **18**, 1004 (1986).
36. M. J. Mumma, M. Misakian, W. M. Jackson, and J. L. Faris, "Angular Distributions and Polarization Fractions of Helium Resonance Radiation ($n\,^1P - 1\,^1S$) in the Extreme Ultraviolet," Phys. Rev. A **9**, 203 (1974).
37. R. L. Kelly and L. J. Palumbo, "Atomic and Ionic Emission Lines Below 2000 Angstroms," NRL Report 7599, Naval Research Laboratory (June 1973).
38. H. Dassen, I. C. Malcolm, and J. W. McConkey, "Polarization of the 104.8 and 106.7 nm Ar Resonance Lines Following Electron Impact Excitation," J. Phys. B **10**, L493 (1977).
39. H. Walker, "High Temperature (Al_2O_3) Insulation and Light Weight Conductors" (Permaluster, Inc., Burbank, CA). See, for example, *Proceedings*, *Conference on High Temperature Electronics*, 25–27 Mar. 1981, Tucson, AZ.

●